University of Texas Rio Grande Valley

ScholarWorks @ UTRGV

12-2012

Synthesis and luminescence properties of core-shell structured (lanthanum(1-x)europium(x))(2)zirconium heptoxid[at]yttrium orthoborate spherical nanoparticles

Suresh Babu Alaparthi
University of Texas-Pan American

SYNTHESIS AND LUMINESCENCE PROPERTIES OF CORE-SHELL STRUCTURED

$(La_{1-x}Eu_x)_2Zr_2O_7$@YBO_3 SPHERICAL NANOPARTICLES

A Thesis

by

SURESH BABU ALAPARTHI

Submitted to the Graduate School of
The University of Texas-Pan American
In partial fulfillment of the requirements for the degree of

MASTER OF SCIENCE

December 2012

Major Subject: Chemistry

SYNTHESIS AND LUMINESCENCE PROPERTIES OF CORE-SHELL STRUCTURED

$(LA_{1-X}EU_X)_2ZR_2O_7$@YBO_3 SPHERICAL NANOPARTICLES

A Thesis
by
SURESH BABU ALAPARTHI

COMMITTEE MEMBERS

Dr. Yuanbing Mao
Chair of Committee

Dr. Elamin E. Ibrahim
Committee Member

Dr. Jason Parsons
Committee Member

Dr. Bimal K. Banik
Committee Member

December 2012

ABSTRACT

Alaparthi, Suresh Babu, <u>Synthesis and Luminescence Properties of Core-Shell Structured</u> <u>(La$_{1-x}$Eu$_x$)$_2$Zr$_2$O$_7$@YBO$_3$ Spherical Nanoparticles</u>. Master of Science (MS), December, 2012, 48 pp., 2 tables, 15 figures, references, 55 titles.

Many rare earth compounds have photoluminescent characteristics for various important applications. In this study, europium doped La$_2$Zr$_2$O$_7$ nanoparticles were first synthesized morphology-controllably by using a molten-salt synthesis method. These nanoparticles were used as the core for coating with YBO$_3$ shell. We then explored the effect of different experimental processing parameters, such as annealing temperatures, reaction times and different ratios of salt mixtures on the structure and morphology of these nanoparticles. The overall core size and shell thickness can be controlled by varying the reactant concentration both the core and shell material. These core@shell nanoparticles were then characterized mainly using power x-ray diffraction, transmission and scanning electron microscopes, and photoluminescence measurements. More importantly, their photoluminescence was carefully studied. These special properties allow these compounds as excellent candidates for broad applications in various devices, such as in lighting devices and radiation detectors.

Key Words: Core-shell nanoparticles, growth kinetics, SEM, TEM and photoluminescence.

DEDICATION

The completion of my master studies would not have been possible without the love and support of my family. My mother, Moulali, my father, Sambaiah, my wife, Venkatalakshmi, my sister, Siva, my father-in-law, Hazarath Babu, and my uncle, Venkateswarlu supported me by all means to accomplish this degree. Thank you for all of your love, patience and support.

ACKNOWLEDGMENTS

TABLE OF CONTENTS

LIST OF TABLES

LIST OF FIGURES

NOMENCLATURE

EDS	:	Energy X-ray dispersive spectroscope
$Eu(NO_3)_3 \cdot 6H_2O$	:	Europium (III) nitrate hexahydrate
FFT	:	Fast Fourier transform
FTIR	:	Fourier transform infrared spectroscopy
KNO_3	:	Potassium nitrate
$La(NO_3)_3 \cdot 6H_2O$	:	Lanthanum nitrate hexahydrate
$NaNO_3$	:	Sodium nitrate
PL	:	Photoluminescence
SEM	:	Scanning electron microscope
TEM	:	Transmission electron microscope
XRD	:	X-ray diffraction
XPS	:	X-ray photoelectron spectroscope
$Y(NO_3)_3 \cdot 6H_2O$	:	Yttrium (III) nitrate hexahydrate
$ZrO(NO_3)_2 \cdot xH_2O$	:	Zirconium(IV) oxynitrate hydrate

CHAPTER I

INTRODUCTION

1.1 History of Nanoscience and Nanotechnology

In 1959, nanotechnology was coined to describe materials in which at least one dimension is less than 100 nm. Physicist Richard Feynman is considered to be the father of nanotechnology. While at the American Physical Society meeting, held in California Institute of Technology, he presented, "There's plenty of room at the bottom". At this meeting he talked about the ideas and concepts behind nanoscience. He mentioned a process how scientists would be able to manipulate and control individual atoms and molecules. Feynman was the first to propose the top-bottom approach, discussed below.[1] Since then, it has been used to describe the interdisciplinary studies by inorganic chemists, organic chemists, materials scientists, and engineers. Nanotechnology is unique in that nanomaterial synthesis, characterization, properties, and application differ from that of the same compound in the bulk phase. It deals with the materials whose structures exhibit significantly novel and improved physical, chemical, and biological properties, phenomena, and functionalities due to their nano-scaled size. Because of their size, nanoparticles have a larger surface-area to volume ratio than macro-sized materials. For example, the intrinsic properties of metal nanoparticles are mainly determined by size, shape, composition, crystallinity and morphology. Nanoparticles, because of their small size, have distinct properties compared to the bulk form of the same material, thus offering many new

1

developments in the fields of electronics, optics, sensors, biomedicine, and bionanotechnology. Nanotechnology is also being utilized in medicine for diagnosis, therapeutic drug delivery and the development of treatments for many diseases and disorders. Nanotechnology is an enormously powerful technology, which holds a huge promise for the design and development of many types of novel products with its potential medical applications on early disease detection, treatment and Prevention.

1.2 Definition

Nanomaterials measured by a small scale of about 1 to 100 nanometers. One nanometer is equal to one-billionth of a meter.

1.3 Approaches of Synthesizing Nanoparticles

Two main approaches for the synthesis of nanomaterials exist: the top-down approach and the bottom-up approach. Top-down methods create nanoscale devices by using larger, externally-controlled ones to direct their assembly. The top-down approach frequently uses the traditional workshop or microfabrication methods where tools are used to cut, mill, and shape materials into the desired shape and size. Top-down methods include micropatterning techniques such as photolithography and inkjet printing. Bottom-up methods create complex assemblies from smaller components. These methods use the chemical properties of compounds to cause single-molecule components to self-organize or self-assemble into nano-sized conformations. The bottom-up approach can produce devices in parallel and yields particles smaller in size than can be synthesized by top-down methods. The desired complexity can be obtained as the assembly is increased. Bottom-up methods are more accepted in the synthesis of nanoparticles.

1.4 Rare Earth Elements

The lanthanide elements are a separate class of seventeen elements in the periodic table including scandium, yttrium, and 4*f* lanthanoids. These elements are often known as the rare earth elements. These elements are the group of elements with atomic number increasing from 57 (lanthanum) to 71 (lutetium). In the periodic table all rare earth elements are in Group IIIb which are separate group due to the filling of the 4f electron shell. In this series, the atomic radii of the lanthanoid elements become smaller as the atomic number increases. This shielding barrier decreases interaction of the *f*-orbitals of the lanthanoid with the energy levels of the free ion which are similar in nature to the energy levels of rare earth in inorganic host complex. In figure 1.1 the various energy levels of the trivalent rare earth ions can be visualized and the energies of emission can be roughly approximated by energy difference between states. The alphanumeric designation next to each level is in accordance to the Russell-Saunders or LS coupling scheme. The labeling formula for each level in the LS coupling is $^{2s+1}L_J$; the s corresponds to the total spin multiplicity, L being the orbital angular momentum, and J representing total angular momentum.

Luminescence phenomena often occur only in the presence of a trace amount of an activator species. Photoluminescence spectroscopy measures the intensity of light emitted by a material over a spectrum of wavelengths after being excited by a monochromatic light source. Photoluminescence is the spontaneous emission of light from a material under optical excitation. The excitation energy, a photon, is absorbed by a material resulting in excitation of an electron from a lower energy state (ground state) to one of higher energy state. While these electrons return to a lower energy states, the excess energy can be released via non-radiative process in the form of phonons. After some time in this state the remaining energy will relax back down to the

ground state, resulting in the emission of a photon. The rare earths that do not have 4f electrons of scandium, yttrium and lanthanum will not show any emissions, while from 58 (cerium) to 71 (lutetium) will have optical efficiency that varies from ion to ion. The f–f energy level transitions are strictly parity forbidden based on the LaPorte selection rules[2], negating the angular momentum (L) between the ground and excited state leading to low molar absorption coefficients on the order of 10 cm^{-1}.
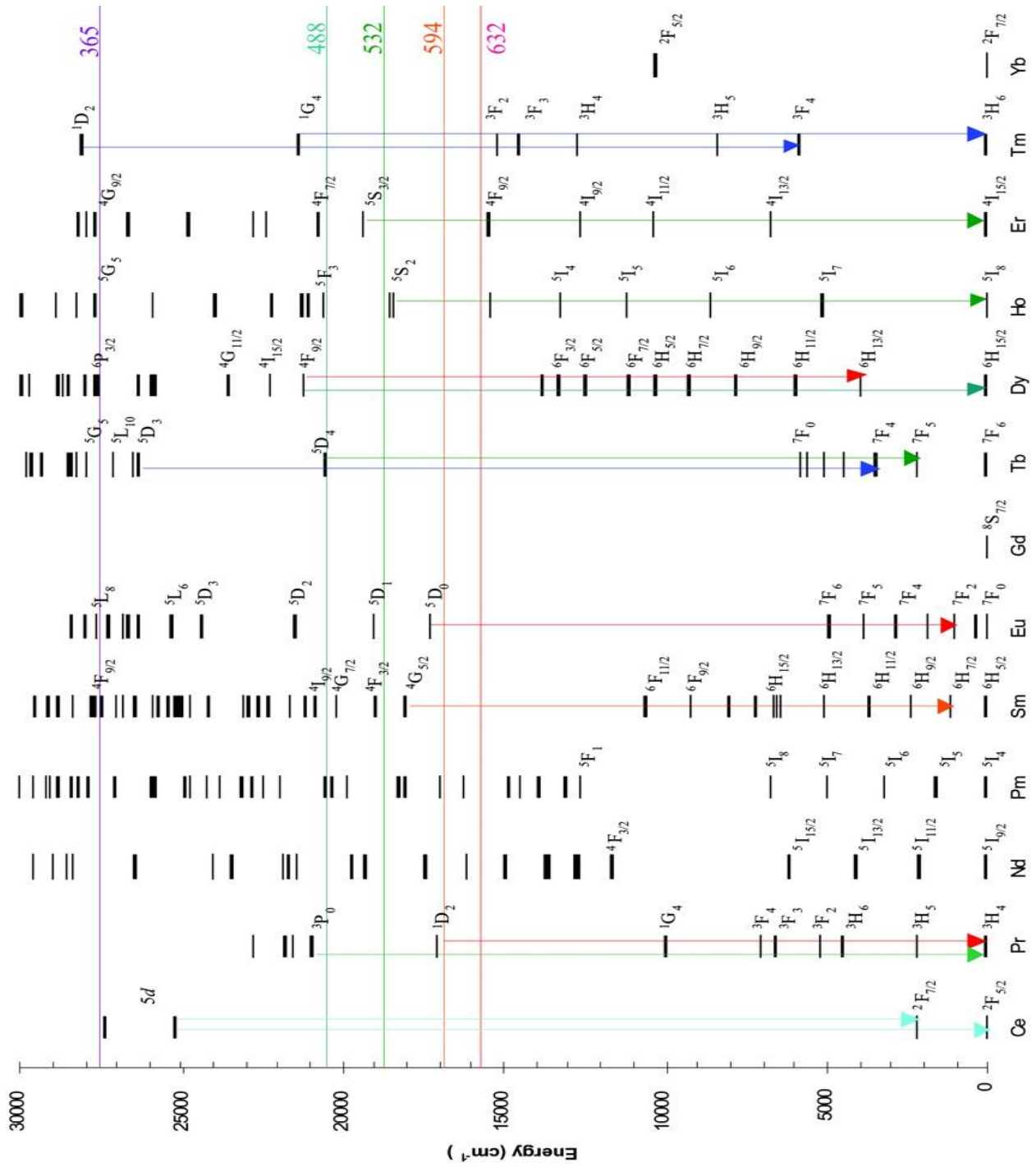
Figure 1.1. The energy diagram for rare earth elements.[3]

1.5 Crystallography
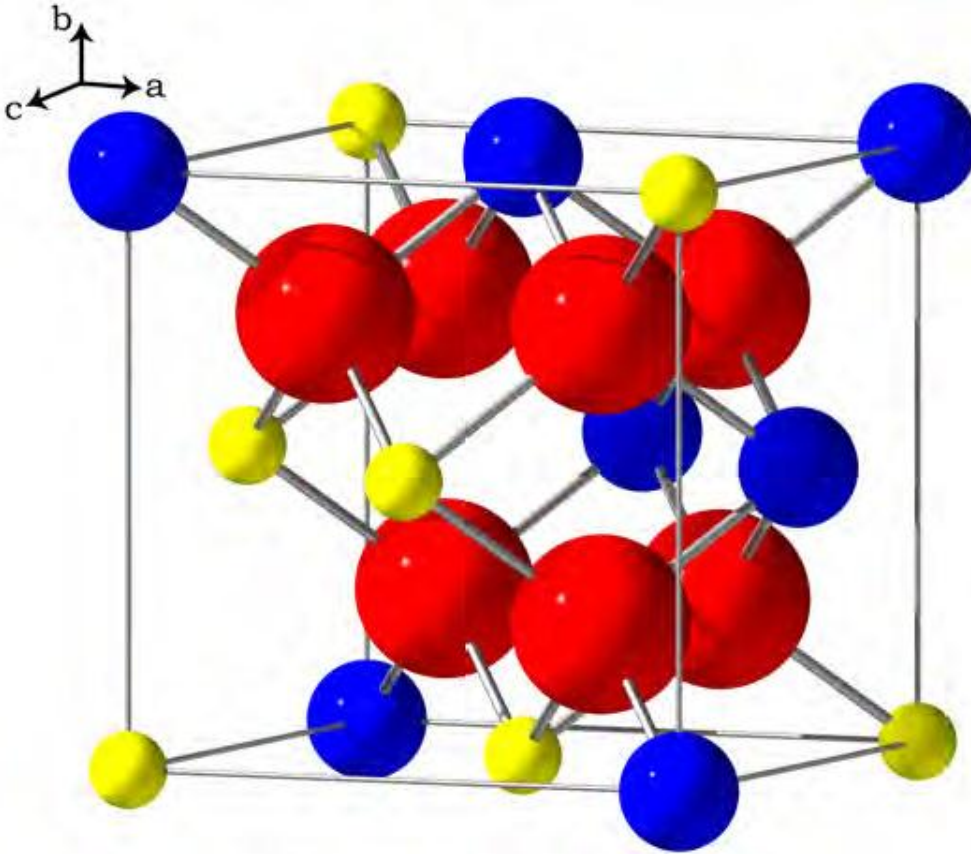
Figure 1.2: The crystal structure of $La_2Zr_2O_7$[4].

$La_2Zr_2O_7$ material contains La^{3+} and Zr^{4+} cations and is a heat-resistant ceramic material. $La_2Zr_2O_7$ composition appropriately written as $La_2Zr_2O_6O'$ to indicate Zr_2O_6 network intersecting with La–O' cations of formula La_2O'. The crystal structure contains corner-shared ZrO_6 octahedra forming the backbone of the network and La^{3+} ions filled in the hexagonal holes in the ZrO_6 octahedra. In this structure, La^{3+} ions can be easily replaced by other rare-earth ions. Both La^{3+} and Zr^{4+} sites can be substituted by a lot of other elements with similar ionic radii in case where electrical neutrality is satisfied. The valence band and the conduction band of $La_2Zr_2O_7$ compound consist of La 4f orbital, Zr 4d orbital and O 2p orbitals. The band structure calculation represents that the La 4f orbitals of $La_2Zr_2O_7$ lie above the top of the O 2p orbitals.

The band gap energy of $La_2Zr_2O_7$ compound size is lower than ZrO_2 because of the effect of 4f orbital electrons.[4]

1.6 Characteristics of Core and Shell

Rare-earth (RE) doped phosphors have been attracted wide attention for optical devices because of their thermal stability, rich luminescence and lifetimes among many attractive spectroscopic properties. All these properties enable RE doped phosphors wide application potentials for a variety of photoluminescence-based lighting, displays, optical networks, signaling, imaging and lasers techniques. Rare-earth ions, with relatively long luminescence lifetimes, have significant advantages for application in fields as varied as lighting optical amplification, scintillating and bioanalysis[5]. The Pyrochlore-type oxides are typically many binary rare-earth and transition metallic elements having the general formula $A_2B_2O_7$. They perform as potential solution for the material research fields[6] and show a wide range of interesting of technological applications including high efficiency catalysis[7], thermal barrier coatings[8,9] conduction of electricity[10], photoluminescence[11], resistance to radiation damage[12]. Lanthanum zirconate offers a set of properties that makes this lattice very attractive for novel high energy radiation detectors. Especially, owing to their high-temperature stabilities and tunable structure, the catalytic properties of pyrochlore oxides have received much attention[13,14,15], possible nuclear waste host materials[16] and have broad application potentials because of their unique and attractive properties.[17] The $La_2Zr_2O_7$ exists in cubic pyrochlore, space group $Fd\text{-}3m$ and $a = 10.785$Å [5]. Some optical properties of Eu^{3+}, Dy^{3+}-doped lanthanum zirconate compounds were previously reported[18]. These materials can be prepared by co-precipitation[19], molten-salt[20], combustion[18,21,22], sol–gel[23], solid-state reaction[24] and hydrothermal synthesis[25].

Recently, there has been a growing interest in strong luminescence of europium ions activated nanocrystals due to their promising applications in fluorescent lamps, field emission display[26] and plasma display panels[27, 28]. Materials activated with Eu^{3+} or Pr^{3+} ions are particularly interested because they often give efficient and fast luminescence resulting from the allowed $5d$–$4f$ transitions of Eu^{3+}/Pr^{3+} ions. The Eu^{3+} ion exhibits simple and well-documented luminescence scheme, it serves as a very efficient and sensitive structural probe and its luminescence, in the case of a non-centrosymmetric environment, is generally dominated by the $^5D_0$–$^7F_2$ transition yielding a red emitting phosphor suitable for lamps and displays[17]. Thus in the present study we used Eu as a substituting, phosphor active element in the $La_2Zr_2O_7$ host lattice. Ionic radius of Eu^{3+} is 0.947Å and La^{3+} is 1.032Å. Hence in the pyrochlore structure Eu^{3+} ions has to substitute La^{3+} with the same valence state and very similar ionic radius, rather than much smaller Zr^{4+} (ionic radius 0.71Å) and Zr^{4+} ions have a different valence. The structure and photoluminescence (PL) properties of the synthesized phosphor were investigated. These nanoparticles are useful in thermal barrier coating applications[8]. Alternative classes of these materials that exhibit unique optical properties are those based on oxides doped rare-earth ions. Among these oxides, the family rare-earth doped lanthanum stannate oxides ($La_{2-x}RE_xSn_2O_7$) used as phosphor materials [29]. Under the Xenon lamp illumination, $La_2Zr_2O_7$ compound shows photocatalytic activity. $La_2Zr_2O_7$ compound behaves as an n-type semiconductor[30] It has a broad application potential due to its unique and attractive properties. This oxide has a relatively high coefficient of thermal expansion, high thermal stability, and low thermal conductivity. $La_2Zr_2O_7$ compound has better chemical resistivity, less oxygen transparency, better bond coat oxidation resistance, higher thermal expansion coefficient, and greater ability to accommodate defects than other rare-earth compounds.[31]

The europium doped $La_2Zr_2O_7$ possesses strong photoluminescence and radiation stability. When europium is doped, the $La_2Zr_2O_7$ crystal lattice is distorted because of the different ionic radii of Eu^{3+} and La^{3+} ions. The emission intensity values of Eu^{3+} ions are high in the $La_2Zr_2O_7$ compound and have an intense photoluminescence due to the f–f transitions. The rare-earth doped pyrochlore $(La_{1-x}Eu_x)_2Zr_2O_7$ had lower thermal conductivity than the undoped $La_2Zr_2O_7$[8].

Yttrium borate (YBO_3) has a hexagonal vaterite-type structure, high chemical and environmental stability, and exceptional optical damage threshold. In 1961, Ernest M. Levin et al.[32] investigated the polymorphism and states of stability of the different structures in yttrium borate at low temperature and the ionic radius.

Yttrium borate is used as shell material in this core-shell nanostructure because of its excellent properties such as high UV transparency, high stability, low stability, and low synthesis temperature. Yttrium borate layers were deposited on europium doped $La_2Zr_2O_7$ spherical particles of various sizes using a sol-gel process, ensuring the formation of core-shell nanostructured europium doped $La_2Zr_2O_7@YBO_3$ spherical particles. These core-shell nanostructured particles will be analyzed and characterized for the luminescence efficiency. These core-shell components will be prepared of solid state inorganic materials, subsequently a more stable and strong system in extreme field environments than other radiation indicators.[32,33] Especially in gamma rays, these core-shell nanostructured particles are prepared to analyze most comfortable mixtures for detecting radiation.

This paper considers that the preparation of Eu doped $La_2Zr_2O_7$ powders has four advantages: (1) the resulting precipitate derived from double hydrous oxides $La(OH)_3ZrO(OH)_2.nH_2O$ is free from contamination, (2) the reaction is carried out under

reasonable conditions, (3) the crystalline powders with a small particle-size distribution show lower agglomeration, and (4) the properties of the particles obtained might be different from those particles crystallized at low temperature. The molten salt synthesis is one of the simplest, most versatile, and highly cost-effective approaches available for obtaining crystalline, chemically pure, single-phase nanoscale materials at lower temperatures and often in overall shorter reaction times with little residual impurities as compared with conventional other synthesis methods. The molten salt synthesis of Eu doped $La_2Zr_2O_7$ powders using La:Eu(OH)$_3$ZrO(OH)$_2$.nH$_2$O as precursor and gives more details of its properties. In the rare-earth, La^{3+} and Eu^{3+} have great luminescence inertia and doped lanthanum zirconate can be used as host material for luminescence. The photoluminescence spectra show the strongest emission at 611 to 615nm corresponding to the electric dipole $^5D_0 \rightarrow ^7F_2$ transition of Eu^{3+} in lanthanum zirconate compound is more useful for display applications.

1.7 Importance of Nanoparticles

Core-shell nanoparticles are constructed of cores and shells of different chemical compositions depending on the application for which the particle is being synthesized. Core-shell nanoparticles are important in size monodispersity, core and shell processibility, tunability, capability of self-assembly and reactivate involving, magnetic, and chemical/biological phenomena. Core-shell nanoparticles need to be functionalized for a lot of interesting reasons for instance, to be effectively used in biomedical and pharmaceutical.[34] Core-shell particles are synthesized for a many important applications in electronics, genomics, and field of display, lighting and bio-nanotechnology.[35] The monodisperse and core-shell composite materials have attracted good optical performance for applications.[36]

1.8 Types of Nanoparticles

Nanoparticles can be classified into many different types such as nanoshell or core-shell particles, pure nanoparticles, hollow particles, and colloidal crystals. Core-shell nanoparticles are composed of a core compound covered by a shell compound. The two compounds often have different characteristics and may combine to produce a composite nanoparticle with properties that are unique from those of both the core compound and the shell compound. Core-shell nanoparticle properties can be modified by changing either the organizing materials or the core-to-shell ratio.

A variety of core-shell particle structures can be synthesized. The main types are represented in Figure 1.3. Figure 1.3(a) represents the surface of a core particle modified by a bifunctional molecule and shell material selectively deposited on the surface of the core particle. Figure 1.3(b) shows shell material deposited on a modified core surface. The shell material formed a complete layer on the core particle. Figure 1.3(c) represents shell material deposited directly on a dielectric core surface. This kind of composite particle can be synthesized by co-precipitation synthesis. Small-sized core particles like gold, platinum, and silver coated with silica material are represented in Figure 1.3(d). Even colloidal particles can be coated by single shell as shown in Figure 1.3(e). Figure 1.3(f) shows a hollow shell particle in which the core particle was removed. Core particles can be removed by either calcinations or dissolution of the core material using a suitable solvent. These kind of hollow particles are known as quantum bubbles. Multiple and concentric nanoshell coating of a dielectric core using a metal shell material is also possible and represented in Figure 1.3(g).[37]

11
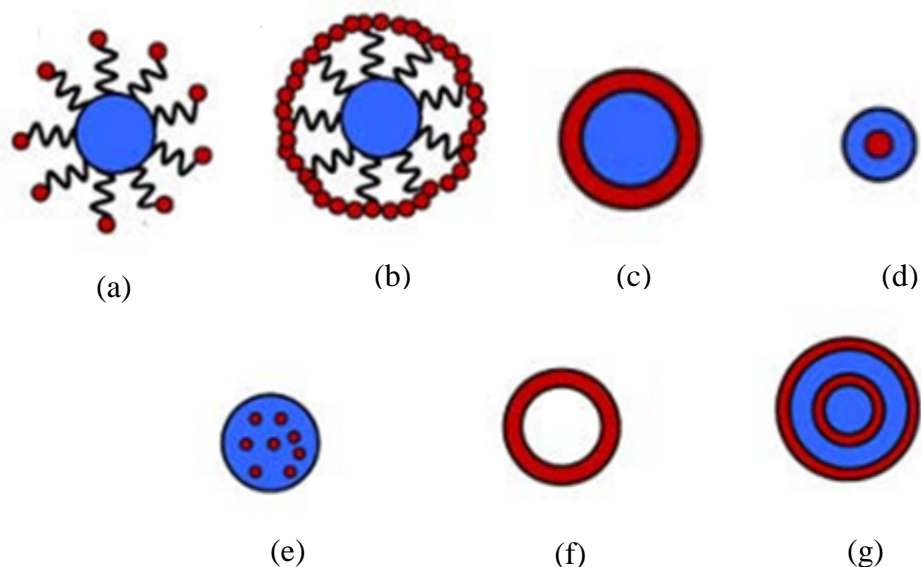
Figure 1.3. Variety of different core-shell particles: (a) surface modified core particle deposited with shell particles, (b) more shell particles reduced onto core to form a complete shell, (c) smooth coating of dielectric core with shell, (d) encapsulation of very small particles with dielectric material, (e) embedding number of small particles inside a single dielectric particle, (f) quantum bubble, (g) multishell particle.[37]

1.9 Classification of Core-Shell Particles

Core-shell particles can be used in a wide variety of applications and serve many different functions depending on their composition. The cores and shells can be made of inorganic or organic materials. Based on the core-shell composition, the core-shell nanoparticles can be classified into four groups: (i) inorganic-inorganic; (ii) inorganic-organic; (iii) organic-inorganic; and (iv) organic-organic. The nanoparticle being synthesized in this experiment falls under the inorganic-inorganic category.

1.10 Inorganic-Inorganic Core-Shell Nanoparticles

Among the types of core-shell nanoparticles, inorganic-inorganic core-shell nanoparticles are the most important class. These types of particles are widely used for the improvement of semiconductor efficiency, information storage, optoelectronics, catalysis, quantum dots, optical

bioimaging, biological labeling, and a variety of other applications. The inorganic-inorganic core and shell components are made of metal, metal oxide, semiconductors, and any other inorganic compound or silica.[38] Metal oxide cores with YBO_3 shells tend to be spherical particles with good optical performance. One example of such a particle is YVO_4 coated with YBO_3. These composite particles have enhanced photoluminescence properties.[39] Core-shell nanoparticles are used for luminescent and radiation applications.

1.11   Core-Shell Nanoparticle Synthesis

Core-shell nanoparticle synthesis involves two main steps. In the first step, the core particles are synthesized. In the second step, the shell is formed on the core particle. A variety of methods exist to accomplish each step.

1.12   Core Synthesis

The core particles are separately synthesized. They are then purified by washing, drying, and annealing. The basic advantage of external core synthesis of core particle is that core particles are in pure form and, hence, there is less possibility of impurities on the core surface. Because any impurities on the surface of the core particle become trapped when the shell is formed, ensuring the purity of the core particle is important.

For inorganic core particle synthesis, the molten-salt, hydrothermal, sol−gel and chemical precipitation reactions in bulk aqueous system are common techniques. For metal-oxide core particle synthesis, the use of the sol−gel method is preferred.[40,41]

1.13   Shell Synthesis

The most important step during the synthesis of core-shell nanoparticles is to maintain uniform coating and to control the shell thickness.

13

1.13.1 Sol−Gel Method

The sol−gel synthesis is a wet-chemical technique widely used in the fields of material science and ceramic engineering for mainly metal oxide particle synthesis. The sol−gel process is an effective method for preparing such materials since the reactants can be homogeneously mixed at the molecular level in solution. Sol-gel processing is synthesis of colloidal dispersions of inorganic and organic-inorganic hybrid materials. From these colloidal dispersions, powders, fibers and thin films can be prepared. The sol-gel technique allows for a low processing temperature and yields molecular level homogeneity.[42,43] This method is mainly used for the synthesis of metal or metal oxide core-shell nanoparticles. This is a hydrolysis of metal salts followed by a condensation process.

1.13.2 Solvothermal Processes

The solvothermal method can be described as a chemical reaction or a transformation of precursors in the presence of a solvent in a closed system and at a temperature higher than the boiling temperature of the solvent. Consequently, pressure is involved. Two different cases are possible: (i) pressure is autogeneous and closely dependent of the percentage of filling for the reaction vessel and of temperature, (ii) pressure is imposed. Solvothermal processes are governed by different key factors: (i) the composition of the reactants, (ii) the nature of the solvent (in particular its physic-chemical properties), (iii) the additives used and (iv) the thermodynamic parameters: temperature and pressure.[44]

1.13.3 Coprecipitation

Coprecipitation is the most commonly used technique to prepare layered double hydroxides (LDHs). In this technique, pH-control conditions can be used during the precipitation step. The pH values are kept constant throughout coprecipitation. At an experimentally-

determined optimal pH, higher crystallinity, smaller particle size, higher specific surface area and higher average pore diameter were found for materials synthesized by co-precipitation. When variable pH and constant pH are compared, the coprecipitation method with constant pH has been used to obtain high crystallinity, phase purity and homogeneity of the materials. [45]

1.13.4 Sonochemical Synthesis

The sonochemistry in synthesis have attracted extensive attention for polymer nanocomposite applications such as in not only academia but also various fields of chemistry, materials science and chemical engineering. The sonochemistry activates and accelerates chemical reactions with acoustic energy, which effectively improves rates of production, reduces reaction time and condition in the sonochemical synthesis.[46]

1.14   Motivation of the Project

In the past decade, most researchers focused on different methods for nanoparticles synthesis. For example, molten salt synthesis is a widely studied method due to its advantages in controlling of particle size and shape. In molten salt synthesis, the mixing of salt and precursors is an important factor to maintain proper composition for formation of desired nanostructured compounds. Salt medium is also play an important role in the formation of nanoparticles. In this project, challenge has been overcome to synthesize lanthanum zircoante and yttrium borate as core-shell nanoparticles. The size of the core nanoparticles was controlled in presence of salt medium.

1.15   Research Goals of the Projects

The main goal of coating the core particles with a shell is to modify the surface of the core particle and to increase its functionality, stability, and dispersal abilities. Core-shell

nanoparticles have broad applications as sensors, photonic crystals, fluorescent diagnostics labels, catalysis while avoiding photo degradation with attractive photoluminescence.[37]

My research work deals with the use of the molten-salt synthesis to create the nanostructure $La_{1-x}Eu_xZr_2O_7$ spherical particles; these particles are used as the core material along with YBO_3 used as the shell. It is expected to demonstrate strong luminescence properties from these core-shell nanostructured samples.

The specific goals are:

1. To optimize the change in europium doped lanthanum zirconate nanoparticle size with variation of salt medium in the presence of precursors.

2. To optimize the effect of europium doping concentrations on photoluminescence in lanthanum zirconate nanoparticle powders.

3. To achieve high luminescence performance with high quenching doping concentration of europium in $(La_{1-x}Eu_x)_2Zr_2O_7$ and $(La_{1-x}Eu_x)_2Zr_2O_7@YBO_3$ nanoparticles.

4. Uniform coating of yttrium borate shell material on the core surface and calculate the overall core–shell nanoparticle size.

5. Characterization of the europium doped lanthanum zirconate core particle and core–shell nanoparticle size by XRD, FTIR, Raman, SEM, TEM, HRTEM, XPS and photoluminescence data.

CHAPTER II

METHOD

2.1 Materials

The starting materials were $La(NO_3)_3.6H_2O$ (99.99%), $Eu(NO_3)_3.6H_2O$ (99.99%), $NaNO_3$ (98%), KNO_3 (99%), $ZrO(NO_3)_2.xH_2O$ (99.9%), $Y(NO_3)_3.6H_2O$ (99.9%), Citric acid (99%), Boric acid (AR), Ammonia (28wt%, AR), and Glucose (99%) from Alfa Aesar USA. Polyethylene glycol (PEG, molecular weight 8000) was obtained from Sigma Aldrich, USA.

2.2 Synthesis

The $(La_{1-x}Eu_x)_2Zr_2O_7$ spherical nanoparticles were prepared according to molten salt synthesis. In a typical synthetic protocol, a single-source complex precursor, i.e., europium doped $La(OH)_3 \cdot ZrO(OH)_2 \cdot nH_2O$, was prepared first by co-precipitation. Lanthanum hexahydrate, zirconium(IV) oxynitrate hydrate (metals basis) and europium(III) nitrate hexahydrate were dissolved in 200 ml of deionized water to from a clear solution, followed by the drop wise addition of 200ml of dilute ammonium solution (concentrated NH_4OH (Alfa Aesar, 28.0−30.0%):H_2O = 1:9 (v/v)). The mixture was stirred vigorously for 2 hr to form a complex precursor europium doped $La(OH)_3 \cdot ZrO(OH)_2 \cdot nH_2O$. The precursor was filtered and washed several times with deionized water and dried at room temperature at least 24 hr. The prepared precursor was mixed with 60 mmol of nitrate mixture by hand grinding with an agate

17

mortar and pestle for 20 min. This mixture was transferred into a covered ceramic crucible and heated to 650°C at a rate of 10°C/min with a box furnace in air and then isothermally annealed at 650°C for 6 hr. After being cooled to room temperature at a ramp-down rate of 10°C/min, the crucible was immersed into deionized distilled water in a beaker to transfer the product into aqueous solution for subsequently separation and purification with about 300 ml of deionized water. Dried in an oven at 110°C overnight, then $(La_{1-x}Eu_x)_2Zr_2O_7$ nanoparticles were obtained.

In a typical experiment, these $(La_{1-x}Eu_x)_2Zr_2O_7$ nanoparticles were coated with carbon to form $(La_{1-x}Eu_x)_2Zr_2O_7@C$ spherical nanoparticles by a hydrothermal synthesis procedure. The $(La_{1-x}Eu_x)_2Zr_2O_7$ nanoparticles were ultrasonicated for 10 min in a diluted ammonia solution (concentrated NH_4OH (Alfa Aesar, 28.0−30.0%):H_2O = 1:9 (v/v)), followed by washing with deionized water. Treated $(La_{1-x}Eu_x)_2Zr_2O_7$ nanoparticles were then redispered in aqueous glucose solution. The mixture was stirred for 30min. After vigorous stirring, the suspension was transferred to an autoclave and kept at 180°C for 4hr and then allowed to cool to room temperature. The black suspension was isolated with deionized water. The final sample was obtained after oven drying at 80°C for 4hr.

Finally, coating with YBO_3 phosphor layers on the $(La_{1-x}Eu_x)_2Zr_2O_7@C$ spherical nanoparticles to obtain the core-shell nanostructured $(La_{1-x}Eu_x)_2Zr_2O_7@YBO_3$ spherical nanoparticles was performed by a sol-gel process. According to compositions in these nanoparticles, stoichiometric amounts of yttrium (III) nitrate hexahydrate, and boric acid, citric acid were dissolved in the water under stirring. Then polyethylene glycol 8000 powder was added. The solution was stirred for 30min and then pH was adjusted to 7.00 by using the dilute ammonia solution. The solution was stirred for 1hr to form a sol and then modified europium doped $La_2Zr_2O_7@C$ spherical nanoparticles were added under stirring. After stirring again for

3hr, the $(La_{1-x}Eu_x)_2Zr_2O_7@C@YBO_3$ spherical nanoparticles were dried at 120°C for 15hr immediately. Then the dried core-shell precursor nanoparticles were annealed to 800°C with ramp-up rate 5°C/min for 2hr. After that, it was cooled to room temperature at a ramp-down rate 5°C/min to form the final $(La_{1-x}Eu_x)_2Zr_2O_7@YBO_3$ spherical nanoparticles.

2.3 Characteristics

2.3.1 X-ray Diffraction

The crystalline structure of the powders was determined using X-ray diffraction with Cu Kα radiation at room temperature by ploting the angular and intensity measurements. The XRD data for the powder samples were examined on a Rigaku-Miniflex^{TM} II X-ray diffractometer using Cu Kα radiation ($\lambda = 0.1549$ nm). The generator voltage and current was set at 35KV and 25mA respectively. The sample was scanned in the 2θ ranges 10° to 90° range in continuous scan mode. The scan rate was 1°/min and step width 0.01° (2ɵ). Phases present in the sample has been identified with the search match facility available with standard measurement software.

Phases present in the sample has been identified with the search match facility available. The crystallite size of the calcined powders was determined from X-ray line broadening using the Scherrer's equation as follows:

$$D_{hkl} = \frac{K\lambda}{\beta Cos\theta}$$

Where, D_{hkl} = the size along the (hkl) direction

K = constant (0.90)

λ = wavelength of the radiation

θ = Bragg's angle and

β = full width at half maximum

2.3.2 X-ray Photoelectron Spectroscopy

Elemental analysis was obtained by XPS. Pressed wafers or cut sections of the samples were attached to stainless steel sample holders using conductive double-sided carbon tape. The chamber was evacuated to a base pressure of ~5 x 10^{-9} Torr. A hemispherical energy analyzer was used for electron detection. XPS spectra were collected using magnesium Kα X-ray source at 80 eV pass energy and in 0.75 eV steps for each sample survey spectrum. Integration and analysis of elemental peak areas in high-resolution spectra were used to generate estimates of the atomic and weight concentrations of the elements present in the samples.

2.3.3 Electron Microscopy

The particle size and morphology of the resulting products were initially characterized using a SEM (ZEISS EVO LS10), Smart SEM software at accelerating voltages of 2kV. The SEM is used to identify the shape and surface of the sample by using ZEISS EVO LS10, Smart SEM software. Specifically, samples were deposited onto conductive copper tape on to carbon conductive tape, which were then attached to the surfaces of SEM brass stubs, so as to minimize charging effects under SEM imaging conditions. For the creation of nameplates samples were initially attached to a piece of double-sided conductive carbon tape copper tape was then used. Specimens for low magnification TEM are obtained by drying droplets of the samples from an ethanolic dispersion onto a 300 mesh Cu grid, coated with a lacey carbon film.

2.3.4 Florescence Spectroscopy

Photoluminescence (PL) emission spectra were taken using a laser diode with excitation wavelength 405nm and USB 2000+ with Sony ILX511B linear silicon CCD array detection range is 340–1050 nm from ocean optics. All samples were scanned for emissions peaks. The emissions scans were mostly in the visible spectrum, from 570 to 720 nm. The sample was mounted on a solid sample holder and angled 90° from the incident light beam so to align

emission signal with the detector. All measurements were done at room temperature. Experimental parameters were set through Thorlab, the controlling software, which also collected the scan data.

2.3.5 Fourier Transform Infrared

Fourier transform infrared (FTIR) spectra of KBr powder-pressed pellets were recorded from 3500 to 400 cm^{-1} with a 4 cm^{-1} spectral resolution on a Thermal Nicolet Nexus 470 spectrometer by signal-averaging 32 scans of a DTGS detector.

2.3.6 Raman Spectroscopy

Raman spectra of powder were recorded from 50 to 900 cm^{-1} with a 4 cm^{-1} spectral resolution on a microscope SENTERRA with laser protective enclosure by signal of CCD detector. The OPUS software is used for instrument control, data acquisitions, manipulation and evaluation.

2.4 Results and Discussion

Previous research on Eu doped $La_2Zr_2O_7$ synthesis involved co-precipitation, solution reaction method, sol-gel, molten-salt and inorganic solid state decomposition of metal nitrate– urea mixtures. All these synthesis processes produced large particles greater than 50nm and smaller surface-area to volume ratio.

In our study, the as-prepared europium doped with $La_2Zr_2O_7$ nanoparticles is pure with no detectable impurities. These diffraction lines observed at 2θ angle 28.89°, 33.71°, 47.94°, 56.80°, 75.36° and 79.12° have been indexed as (222), (400), (440), (622), (444) and (800) respectively, these peaks are characteristic of fluorite structure. The XRD patterns were analyzed to determine peak intensity, position and width. Full-width at half-maximum (FWHM) data was used, and the average particle size was estimated using Scherer equation (discussed in 'Material and Methods' section 2.1.1). The typical XRD pattern revealed that the sample contains a fluorite phase

structure of europium doped lanthanum zirconate particles nanoparticles. The average estimated particle size of this sample was 20 ± 3 nm derived from the FWHM of peak corresponding to (222) plane. All the peaks indicate a cubic phase of $La_2Zr_2O_7$ and approximately close to the reported information (JCPDS 17-450). No obvious XRD peaks arising from impurities were found, meaning that $(La_{1-x}Eu_x)_2Zr_2O_7$ nanospheres were successfully synthesized with high purity. By indexing the XRD patterns, the data from our as-synthesized $(La_{1-x}Eu_x)_2Zr_2O_7$ with different dopant concentrations are shown in Figure 2.1. From their respective cubic phases, the pure $La_2Zr_2O_7$ had calculated cell constants of 10.765 Å, which is in agreement with the standard JCPDS 17-450.
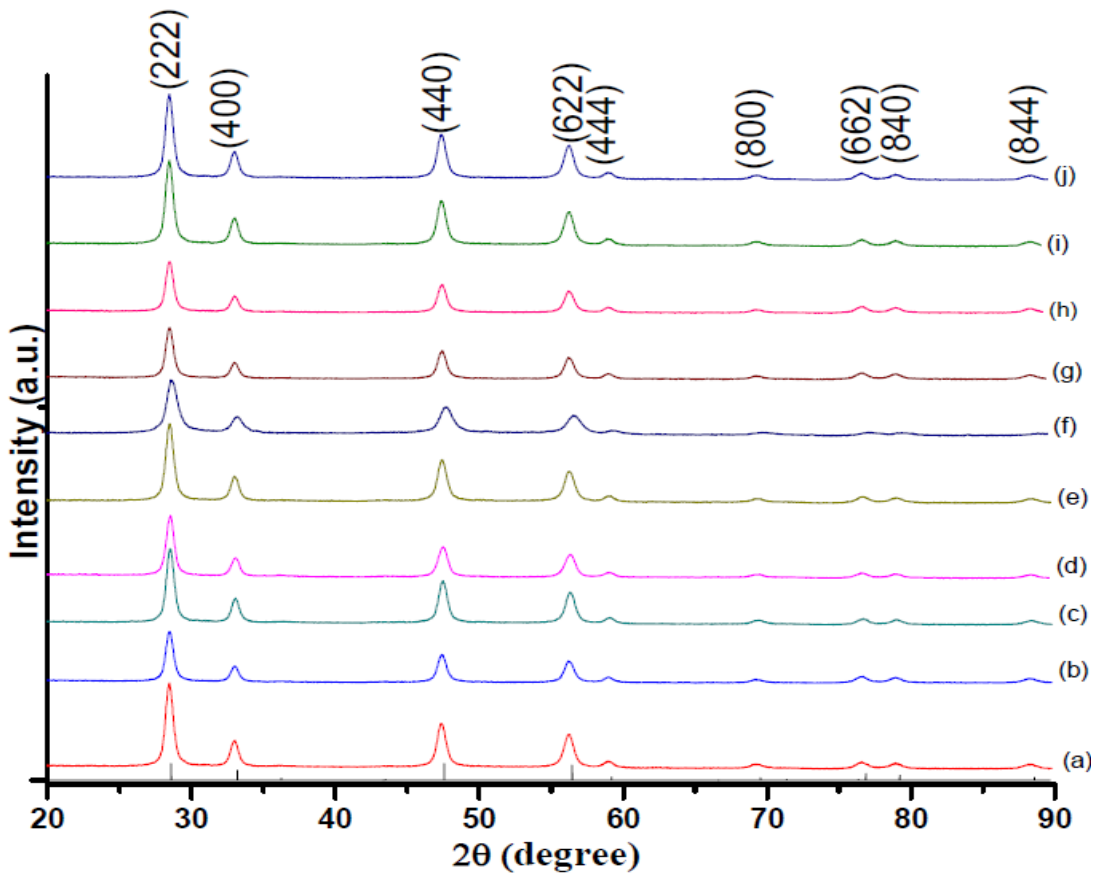
Figure 2.1: XRD patterns of Eu^{3+} doped $La_2Zr_2O_7$ powders heated at 650°C temperature with different doping concentrations (a-j) 0, 1, 2.5, 5, 8, 9, 10, 11, 15, 20% Eu concentrations.

As shown in Figure 2.2, as-prepared the YBO_3 shell exhibit single phase of XRD pattern, indicating a pure phase with no detectable impurities. All the peaks were approximately close to the reported information (JCPDS 16-277).
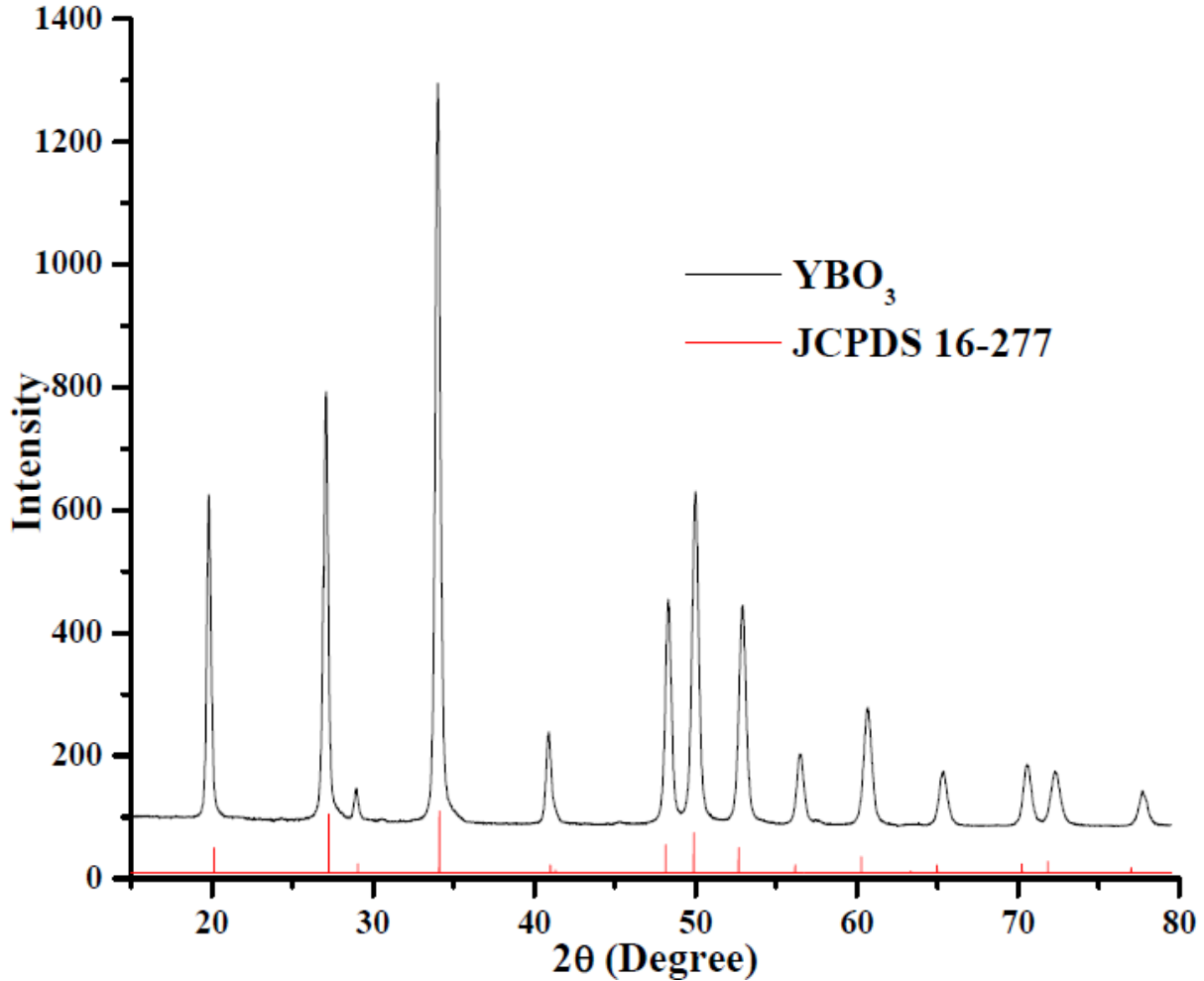
Figure 2.2: The XRD pattern of YBO_3 shell

As shown in Figure 2.3, the $(La_{1-x}Eu_x)_2Zr_2O_7@YBO_3$ core/shell exhibit two phases of XRD patterns, namely, those of $(La_{1-x}Eu_x)_2Zr_2O_7$ and YBO_3. In addition, the intensities of the peaks of YBO_3 increase with the shell ratio. Therefore, the nanostructures are composed of the $(La_{1-x}Eu_x)_2Zr_2O_7@YBO_3$, which is in agreement with the standard JCPDS 17-450 and JCPDS 16-0277.
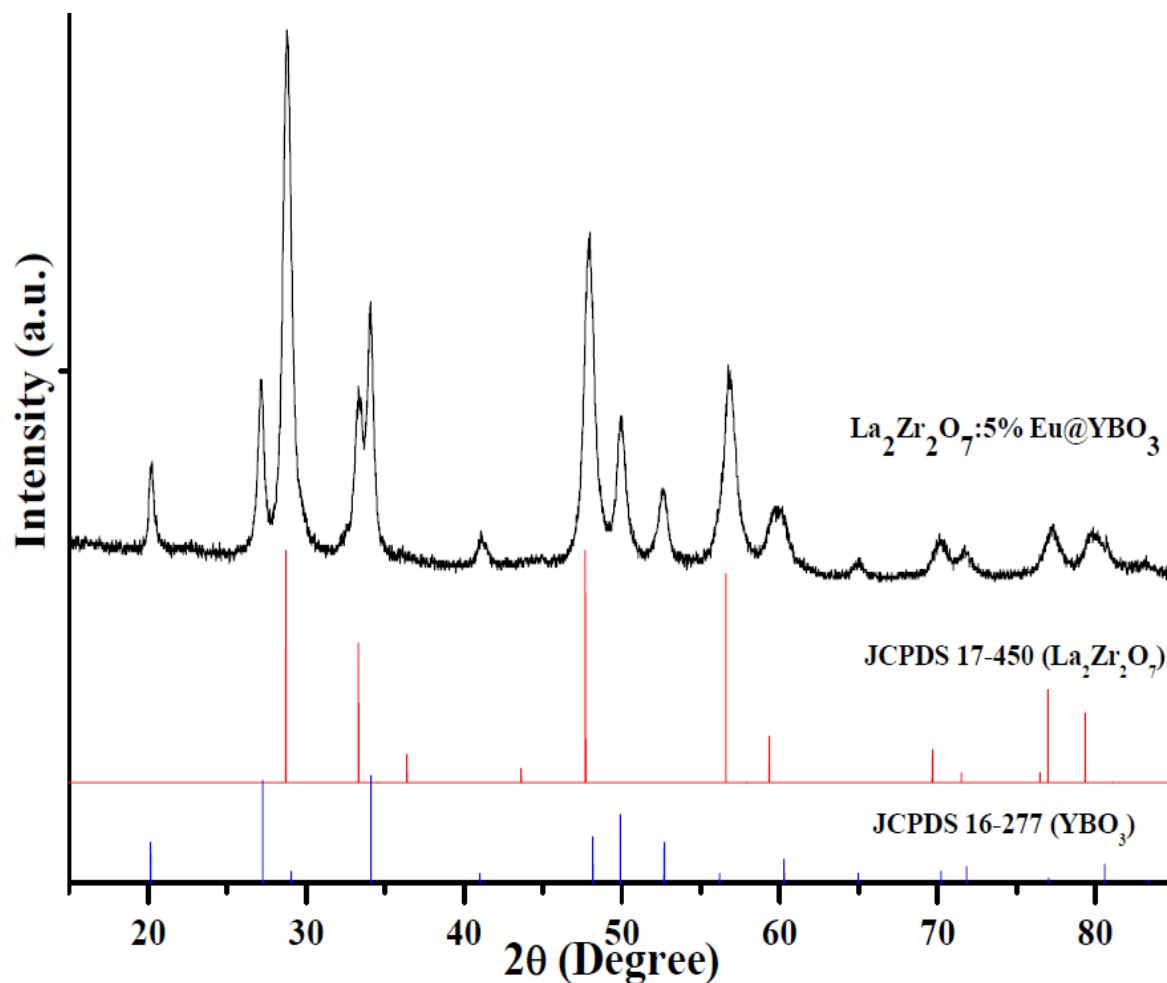
Figure 2.3: The XRD pattern of $(La_{1-x}Eu_x)_2Zr_2O_7@YBO_3$ nanoparticles.

The sizes and morphologies of as-prepared samples were examined by both scanning and transmission electron microscopic techniques. Figure 2.4 shows the SEM images of the as-prepared nanoparticles. Fig 2.4(a) shows undoped $La_2Zr_2O_7$ spherical nanoparticles, Fig 2.4(b) shows 2.5%Eu-doped $La_2Zr_2O_7$ spherical nanoparticles, Fig. 2.4(c) shows the 2.5%Eu-doped $La_2Zr_2O_7@C$ core-shell spherical nanoparticles, and Fig. 2.4(d) shows the coresponding 2.5%Eu-doped $La_2Zr_2O_7@YBO_3$ core-shell spherical nanoparticles. The SEM images shows that the as-formed $(La_{1-x}Eu_x)_2Zr_2O_7$ samples consist of spherical particles with an average size of 20 $\pm$ 3 nm (based on 50 particles each), and these particles are nonaggregated with narrow size distrubution.
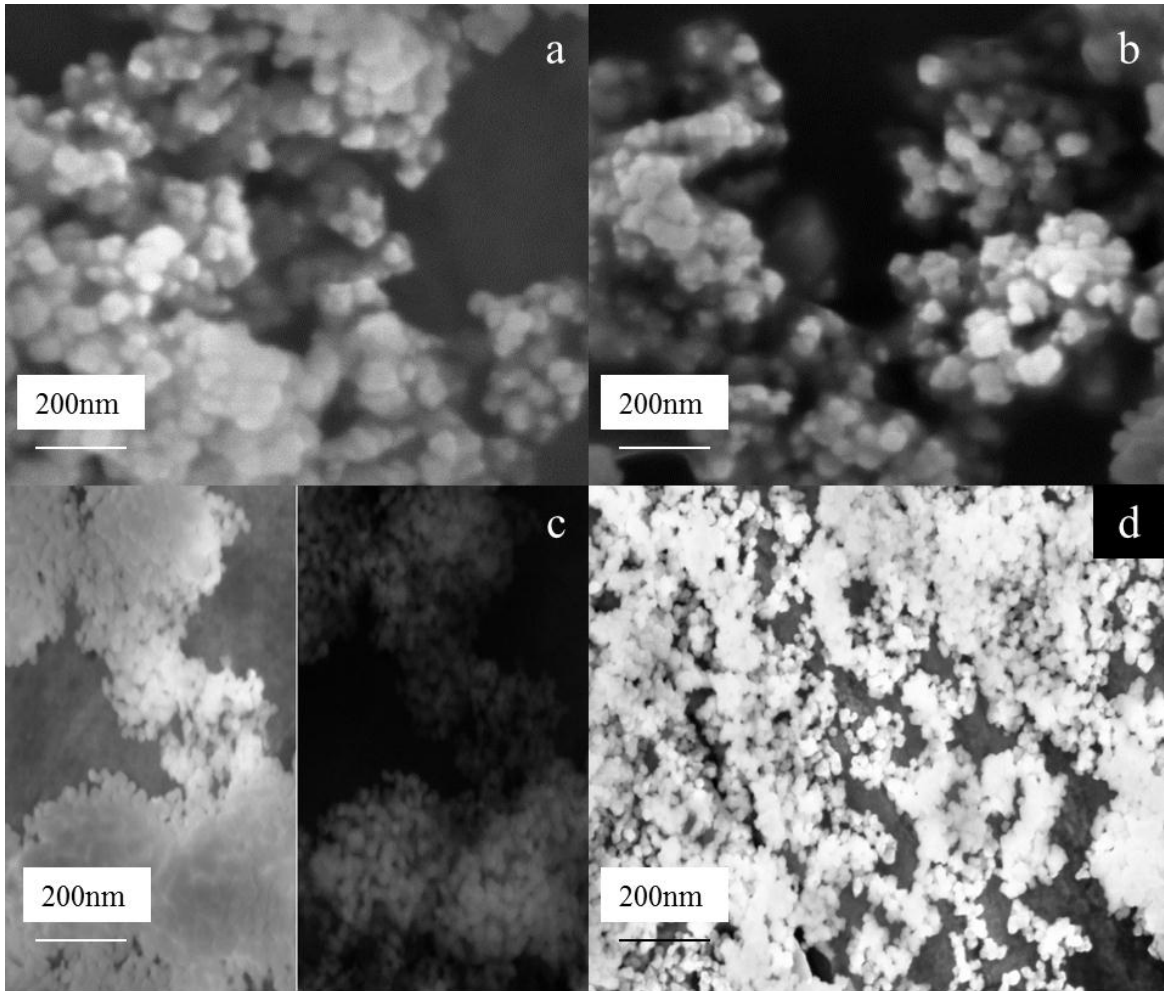
Figure 2.4 SEM images of as-synthesized (a) $La_2Zr_2O_7$, (b) $(La_{1-x}Eu_x)_2Zr_2O_7$, (c) $(La_{1-x}Eu_x)_2Zr_2O_7@C$, and (d) $(La_{1-x}Eu_x)_2Zr_2O_7@YBO_3$ nanoparticles.

Fig. 2.5(a-c) show general low-magnification TEM images of europium doped lanthanum zirconate nanoparticles. These images demonstrated that $(La_{1-x}Eu_x)_2Zr_2O_7$ nanoparticles with particle size of 20 ± 3 nm (based on 50 particles each), were prepared by the molten-salt synthetic procedure at a temperature of 650°C. They are mostly spherical, and some of them have clear edges. It is also easy to tell that our as-synthesized $(La_{1-x}Eu_x)_2Zr_2O_7$ nanoparticles are well dispersible, unlike those prepared by different synthesis[18,19,23,47]. In our synthetic process, the molten salt mixture used acts as a salt medium between the formed nanoparticles or

25

surfactant on the nanoparticles surface. It prevents them from agglomerating during the nanoparticle growth process, and even during the cooling process. A typical HRTEM image is shown in Fig. 2.5(d). Fig. 2.5(d) shows that the lattice orientation of an individual nanoparticle can be seen clearly, which indicates the presence of single-crystalline. The appearances of these nanoparticles are basically flat though some of their corners and edges are a little truncated. The shape of these nanoparticles is likely determined by the comparative exact surface energies of the facets. The HRTEM images shows that regular succession of the atomic planes, which belongs to different planes of the lattice. The clear and regular crystal lattice distances suggest that highly crystalline $La_2Zr_2O_7$ are formed. The $La_2Zr_2O_7$ nanoparticles, the corresponding FFT pattern indicates the regular diffraction spots, which indicates that $La_2Zr_2O_7$ nanoparticles with good crystallinity are polycrystalline. These lattice images of individual nanoparticles also show that they are crystalline. The lattice fringe with the interplanar distances measured from Fig. 2.5(d) are 0.310 nm, which are consistent with the theoretical values $d_{222} = 0.311$ nm of the $La_2Zr_2O_7$ structure. It suggests that high quality $La_2Zr_2O_7$ nanoparticles were formed. This results perfectly matches JCPDS 17-450 identified by XRD analysis. Moreover, this calculation can be confirmed by the angle between two planes as indexed in Figure 2.5(d).
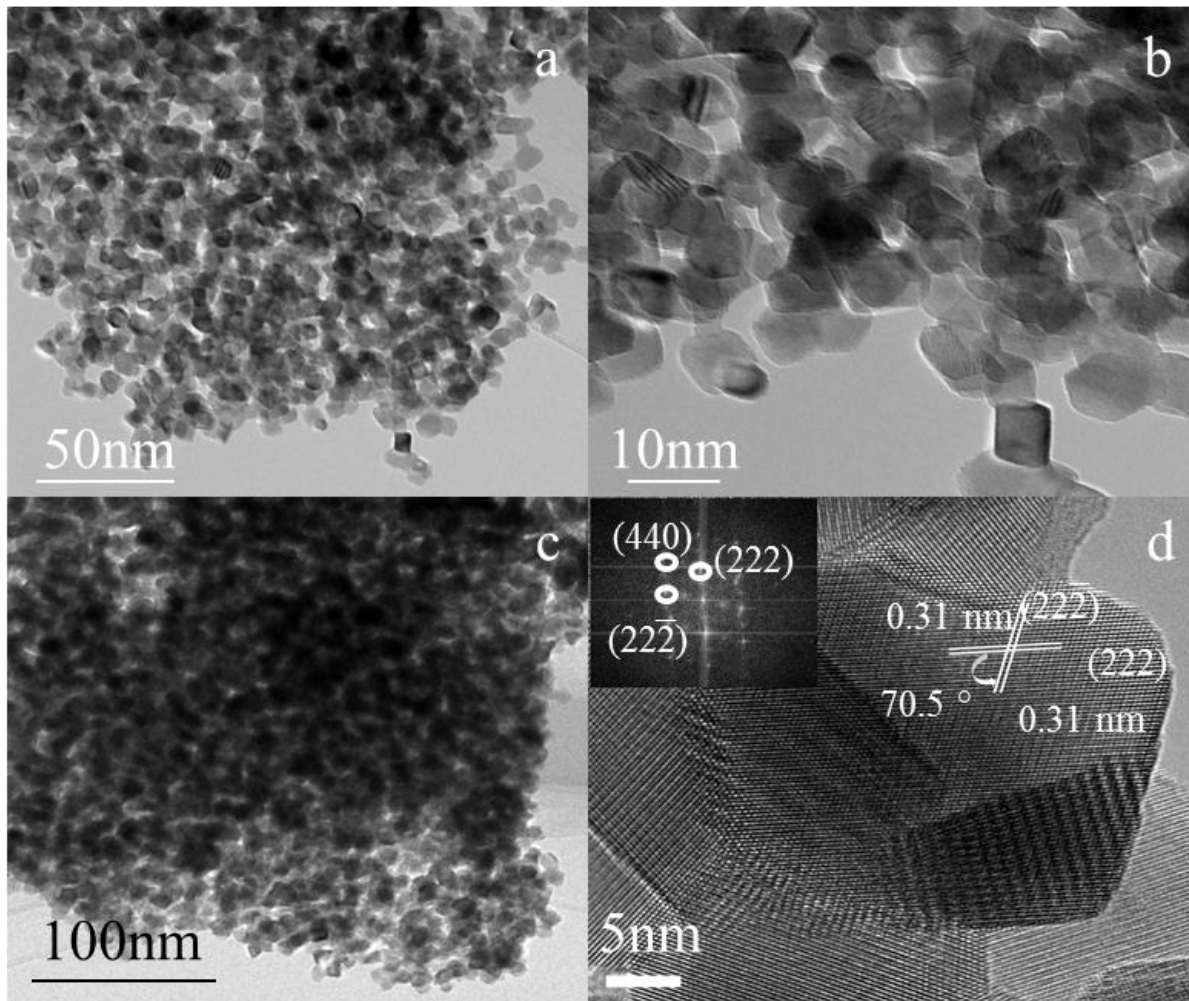
Figure 2.5 HRTEM and TEM images of as-prepared $(La_{1-x}Eu_x)_2Zr_2O_7$

The energy dispersive spectra of all the samples prepared at 650 °C are recorded. The corresponding EDS spectrum of the $(La_{1-x}Eu_x)_2Zr_2O_7@YBO_3$ shown in Figure 2.6 are composed of the elements of La, Zr, Eu, Y, B and O, as expected.
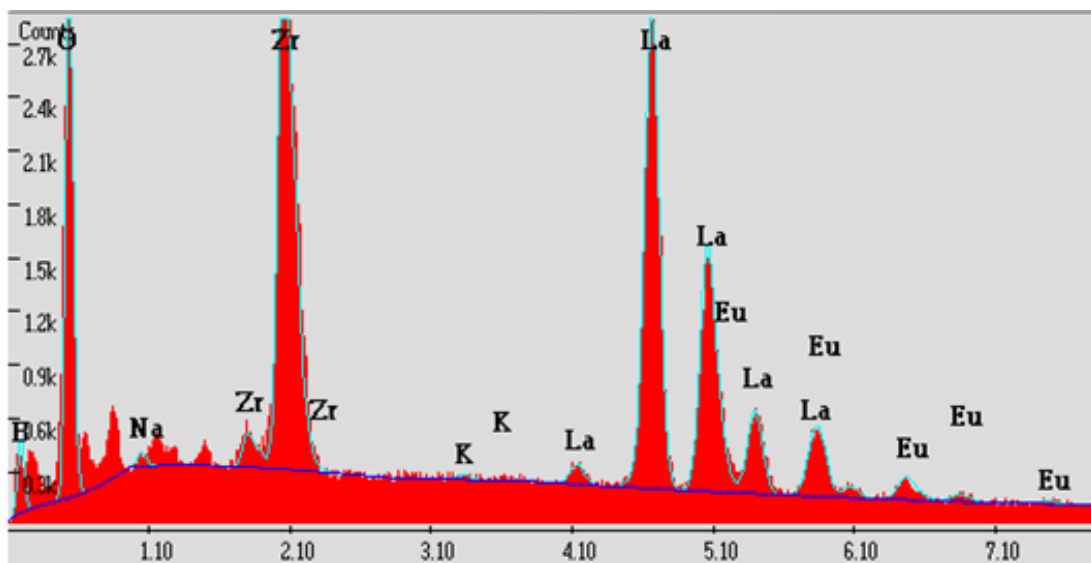
Figure 2.6 EDAX spectra of as-prepared $(La_{1-x}Eu_x)_0Zr_2O_7$

The X-ray photoelectron spectra of $(La_{1-x}Eu_x)_2Zr_2O_7@YBO_3$ core-shell spherical nanoparticles are shown in Figure 2.7. These spectra exhibit characteristic Ln $3d$, Zr $3d$, Eu $4d$, Y 3d, B 1s and O1s peaks. The $3d$ peak of lanthanide splits into $3d_{5/2}$ and $3d_{3/2}$ due to spin–orbit coupling, which varies from $\sim$17 eV for La to $\sim$37 eV for Dy. In case of europium doped lanthanum zirconate, the La $3d$ profiles exhibit asymmetric peaks at 839 and 856 eV which are assigned to $3d_{5/2}$ and $3d_{3/2}$ levels of La^{3+}. The Zr $3d_{5/2}$ and $3d_{3/2}$ peaks were observed at 183 and 186 eV, respectively, and spin–orbit coupling was found to be 2eV. The Eu $3d$ profiles exhibit asymmetric peaks at 1118 and 1134eV which are assigned to $3d_{5/2}$ and $3d_{3/2}$ levels of Eu^{3+}. The B1s peaks were observed at 183 and 196eV. The O1s peaks were observed at 533.1and 530.6eV. These data are consistent with the oxidation states of La and Zr, as being +2 and +4, respectively, which are expected of $(La_{1-x}Eu_x)_2Zr_2O_7$ formation.

28
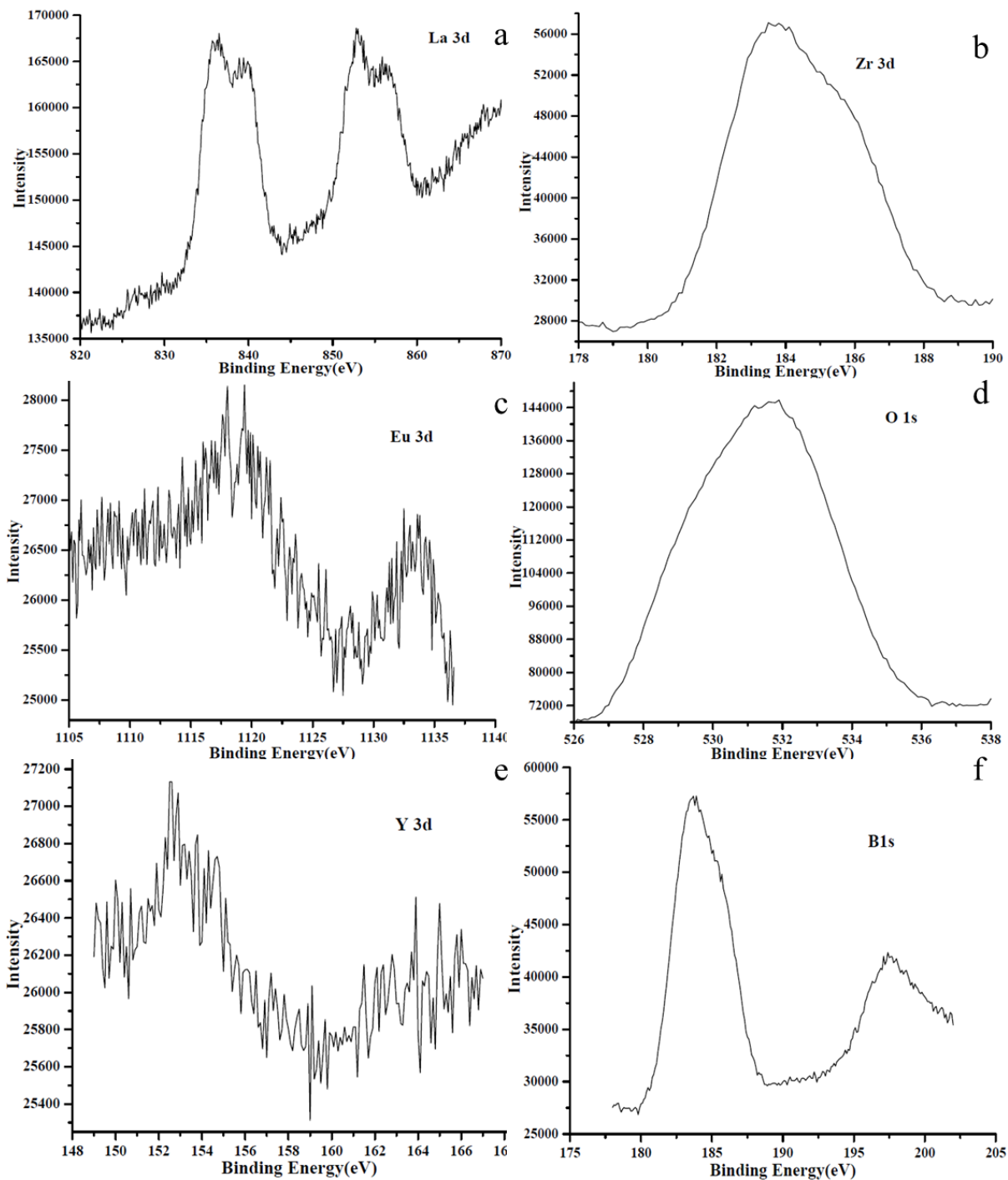
Figure 2.7 XPS spectra of europium doped lanthanum Zirconate coated with yttrium borate nanoparticles.

The IR spectrum of the europium doped lanthanum zirconate nanoparticles shows in Fig. 2.8(a). The characteristic absorption of at 568 cm^{-1} and 492 cm^{-1} corresponding to the

vibrational mode of ZrO_6 and LaO_8 polyhedra[23,25]. The band located at 1372.39 and 1503.91 cm^{-1} assigned to absorption of La_2O_3[23]. The IR spectrum of the europium doped lanthanum zirconate coated with yttrium borate nanoparticles shows in Fig. 2.8(b). The IR absorption peaks between 800 and 1200 cm^{-1} are typical for the polyborate group $B_3O_9{}^{9-}$.[48,49] The IR absorption peaks in the region of 800−950 cm^{-1} are assigned to ring-stretching vibration modes and the peaks in the region of 950−1200 cm^{-1} are assigned to terminal-stretching vibration modes confirm to previous reports.[48, 50]
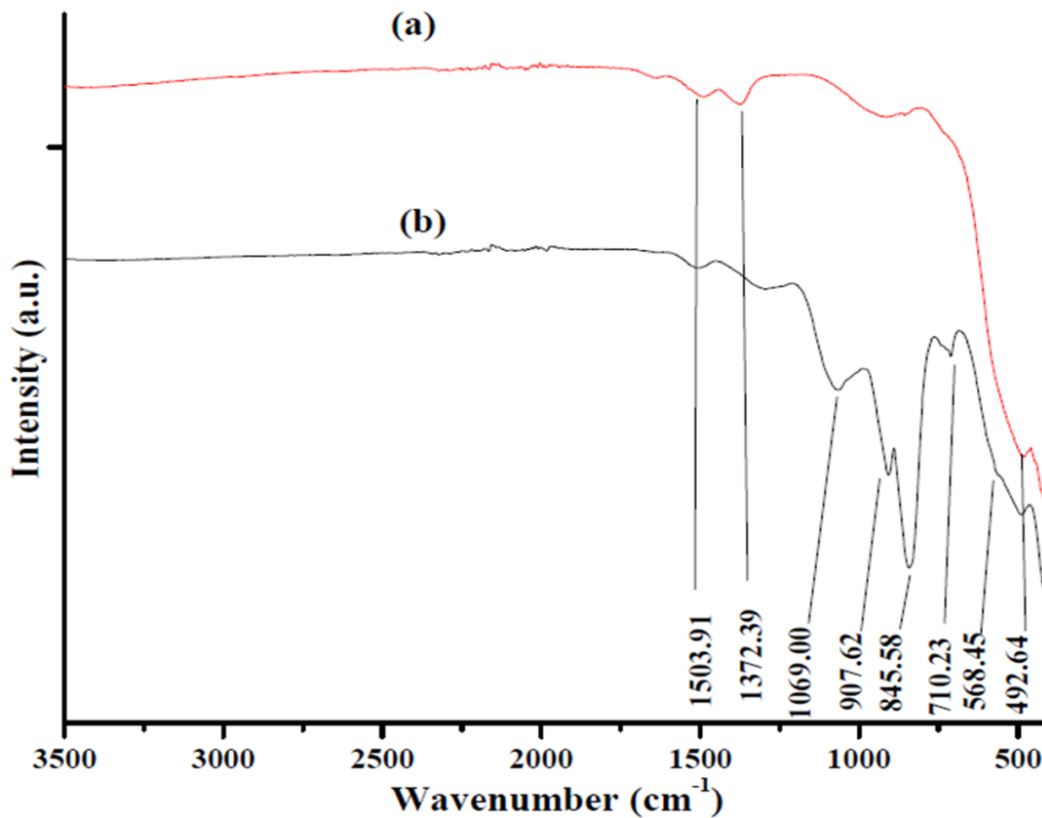
Figure 2.8: The FT-IR spectra of $La_2Zr_2O_7$:Eu and $La_2Zr_2O_7$:Eu@YBO_3

The Raman bands at 300.5 cm^{-1} and 395.45 cm^{-1} are attributed to the stretching mode of the La-O and Zr-O respectively. The Raman spectrum of YBO_3 reported in Fig. 2.9 shows the peak at 513 cm^{-1}. This peak is not able to be attributed to the internal modes of the BO_4 polyhedron and is probably due to the lattice modes corresponding to Y−O stretching vibrations.
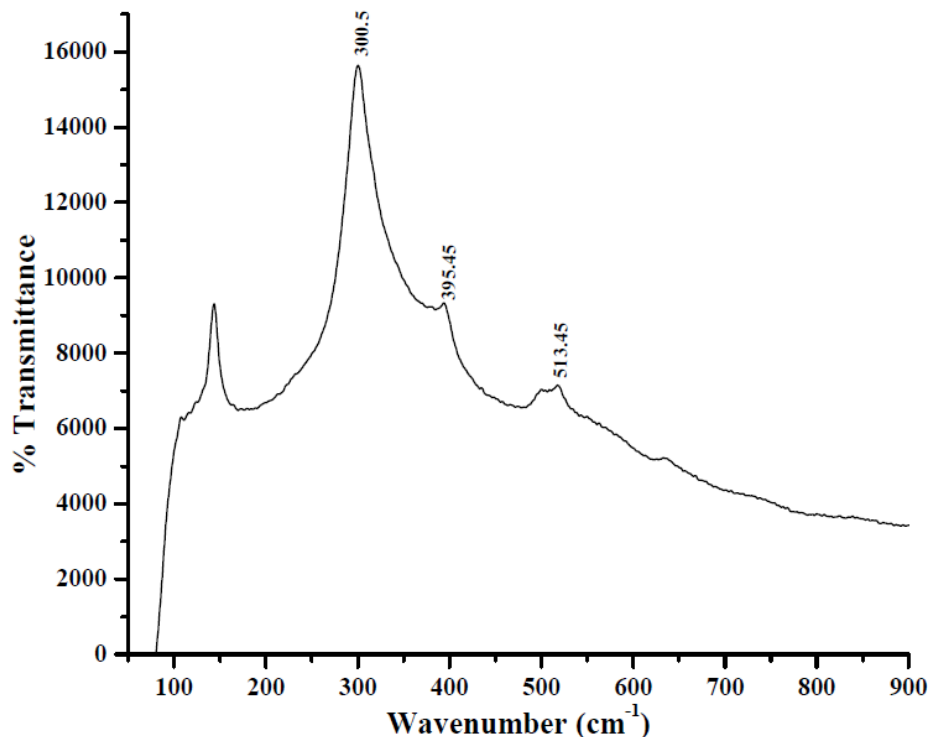
Fig. 2.9. Raman spectrum of europium doped lanthanum zircoante nanoparticles.

A sample spectrum is shown in Fig. 2.10. Photoluminescence (PL) emission spectra excited the series $La_2Zr_2O_7$:Eu with different dopant contents. Emission spectra for the compound are taken using an excitation wavelength of 405 nm. The europium-doped lanthanum zirconate showed strong luminescence due to *f-f* transition lines within the Eu^{3+} ($^4f_6$) electron emission configuration. The overall energy level structure of the Eu^{3+} ions does not change in different phosphors due to the shielding effect of the $5s^2 5p^6$ electrons. In such a situation the spectra simply reflect the variety of symmetry sites the Eu^{3+} occupy. The emission peak at 590 nm is assigned for magnetic dipole transition, $^5D_0-{}^7F_1$. The largest peak emission line at around wavelength 611 and 630 nm is assigned to the hypersensitive $^5D_0 \rightarrow {}^7F_2$ transition and peak at 710 nm to $^5D_0-{}^7F_4$ transition using a forced electric dipole transition mechanism. It is indicated that the Eu^{3+} ions in the La^{3+} sites were preferentially excited at 405 nm ($^5D_2 \rightarrow {}^7F_0$) energy level. Because Eu^{3+} and La^{3+} ions have near-ionic radii and exhibit no charge compensation, the two

31

cations can substitute readily for each other in the $La_2Zr_2O_7$:Eu. As shown clearly in Fig. 2.10, the peaks the $^5D_0 \rightarrow {}^7F_2$ transition are much stronger than those the $^5D_0 \rightarrow {}^7F_1$ transition due to the lower symmetry of Eu^{3+} sites. Accordingly, it is more promising to use good crystallinity of the $La_2Zr_2O_7$:Eu nanoparticles and low distortion from inversion symmetry environment for the Eu^{3+} sites in the host lattice. The electronic dipole transitions allowed only at low symmetries when the luminescent ion is in a site without inversion symmetry and magnetic dipole transitions dominate when Eu^{3+} is located in a site with inversion symmetry. To understand multiband emissions, site symmetries should be lowered to certain extent by chemical modification of hosts through introducing lattice defects. There is no splitting around 575 nm noticed in the emission spectra indicating that the Eu^{3+} ions occupied only one site, i.e. the Eu^{3+} ions were located in the site with D_{3d} symmetry because of the same valence and similar ion radius, which has a highly asymmetric environment, the electric dipole transition becomes very strong compared to that of magnetic dipole transition[51]. Fig. 2.10 shows the normalized luminescence emission spectra of Eu^{3+} (Eu^{3+} = 0, 1, 2.5, 5, 8, 9, 10, 11, 15 and 20 at. %) doped $La_2Zr_2O_7$ nanoparticles excited at 405 nm respectively. For comparison, all the luminescence spectra are normalized at 611.45 nm. Intensity increases and then decreases with increasing doping levels up to 20%. The concentration quenching occurs in 10mol% Eu^{3+} doped lanthanum zirconate nanoparticles.
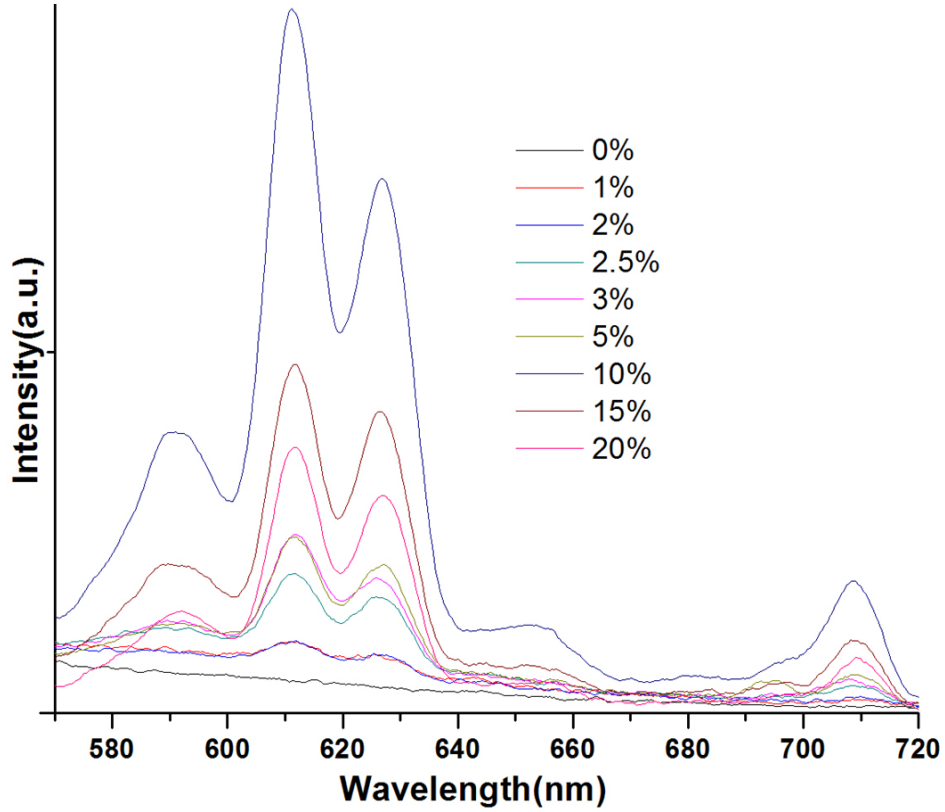
Figure 2.10: Luminescence emission spectra of Eu^{3+} (Eu^{3+} = 0, 1, 2.5, 5, 8, 9, 10, 11, 15 and 20 at. %) doped $La_2Zr_2O_7$ nanoparticles excited at 405nm.

To get intensity of emission at magnetic and electric dipole transitions, there is a need to fit with suitable distribution functions. The magnetic and electric dipole transitions by using the Gaussian distributions:

$$I = I_B + \frac{A}{W\sqrt{\pi/2}}e^{-2\frac{(\lambda-\lambda_C)^2}{w^2}}, \text{ (52)} \tag{1}$$

Where I is intensity, I_B is the background intensity, A is the area, w is the width of the curve taken at half maximum. λ is the wavelength and λ_c is the mean value corresponding to transition. These are fitted in the range 601–619 nm. The typical fitting to the electric dipole transitions data of 10 at. % Eu^{3+} doped $La_2Zr_2O_7$ nanoparticles prepared at 650 °C after excitation at 405 nm. It fits well with $\chi2 = 0.98$ Values of the fitting parameters I_0, A, w, and λc are 0,

48547.01(counts), 9.44, and 611.78 nm, respectively. In-details values such as the peak positions of the electric dipole transition $^5D_0{\rightarrow}^7F_2$ and FWHM of all as prepared, Eu^{3+} doped $La_2Zr_2O_7$ samples after fitting with Gaussian distribution are given in Table 1.

Table: 1 Peak position of the electric dipole transition ($^5D_0{\rightarrow}^7F_2$) and FWHM (*w*) of as prepared, 650 °C heated Eu^{3+} doped $La_2Zr_2O_7$ samples.

Eu^{3+} (at. %)	Peak width of the curve electric dipole transition at $^5D_0{\rightarrow}^7F_2$(611 nm)
1	10.76
2.5	8.40
5	8.64
8	8.63
9	9.10
10	9.44
11	9.08
15	9.09
20	9.01

The peak positions of Eu^{3+} emissions (electric dipole allowed transitions) are not affected but FWHM value decreases slightly as doping increases. Fig. 2.11 shows the intensity area of electric dipole allowed transition versus Eu^{3+} concentration curve of Eu^{3+} doped $La_2Zr_2O_7$:Eu nanoparticles obtained by Gaussian curve fitting. All the spectra were recorded by exciting at 405 nm, respectively. This clearly reveals that there is a significant change in the area of the doping samples where the maximum is found in the 10 at.% of Eu^{3+} and then decreases due to concentration quenching effect on further increase in Eu^{3+}. However, no such change is observed in the as prepared sample.
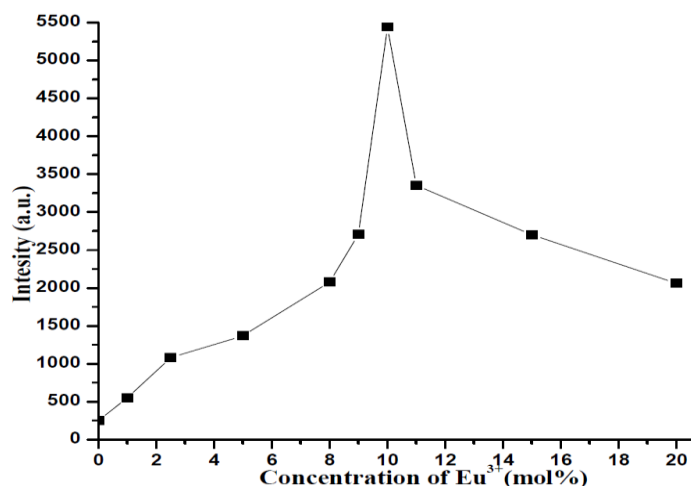
Figure 2.11. Intensities of electric dipole transitions (601–619 nm) vs Eu^{3+} concentrations of as prepared, Eu^{3+} doped La$_2$Zr$_2$O$_7$ nanoparticles excited through 405 nm.

The comparison of core and core shell nanoparticles emission spectra as shown in the Fig. 2.12. As shown in this figure, both the emission spectra of La$_2$Zr$_2$O$_7$:Eu nanoparticles and the La$_2$Zr$_2$O$_7$:Eu@YBO$_3$ nanoparticles shows two well-known PL emission bands in the range of 580–720 nm. The orange emission centered at 595 nm was assigned to the $^5D_0 \rightarrow {}^7F_1$ transition of Eu^{3+},[53] the red emission at 615 nm was due to the $^5D_0 \rightarrow {}^7F_2$ transition. As a result, the red emission from electric dipole $^5D_0 \rightarrow {}^7F_1$ transition is relatively strong, which is allowed in the inner electronic configuration and is hardly influenced by the environment of the Eu^{3+} activators. The two emission bands at 590 nm and 611 nm are assigned to the magnetic-dipole transition $^5D_0 \rightarrow {}^7F_1$ of Eu^{3+} at 590 nm and the forced electric-dipole transition $^5D_0 - {}^7F_2$ of Eu^{3+} at 611 nm, respectively. In this synthesis, the $^5D_0 \rightarrow {}^7F_2$ emission at 611 nm is selected as a standard to determine their relative PL efficiency. The La$_2$Zr$_2$O$_7$:Eu@YBO$_3$ nanoparticles display a stronger PL emission than the La$_2$Zr$_2$O$_7$:Eu sample, because the of the La$_2$Zr$_2$O$_7$:Eu nanoparticles was coated with YBO$_3$ shell in the core-shell process. Fig.2.12 expresses that all the La$_2$Zr$_2$O$_7$:Eu@YBO$_3$ except for those with the shell shows much stronger photoluminescence

than the $La_2Zr_2O_7$:Eu nanoparticles under the same conditions.[33] The $La_2Zr_2O_7$:Eu@YBO_3 shows the highest PL efficiency, whose photoluminescence intensity of the $^5D_0 \rightarrow {}^7F_2$ emission is 30% higher than that of the $La_2Zr_2O_7$:Eu nanoparticles because dependence of transitions on the activator concentration. Therefore, PL efficiency of $La_2Zr_2O_7$:Eu nanophosphor can be improved by forming $La_2Zr_2O_7$:Eu@YBO_3 core/shell nanoparticles.
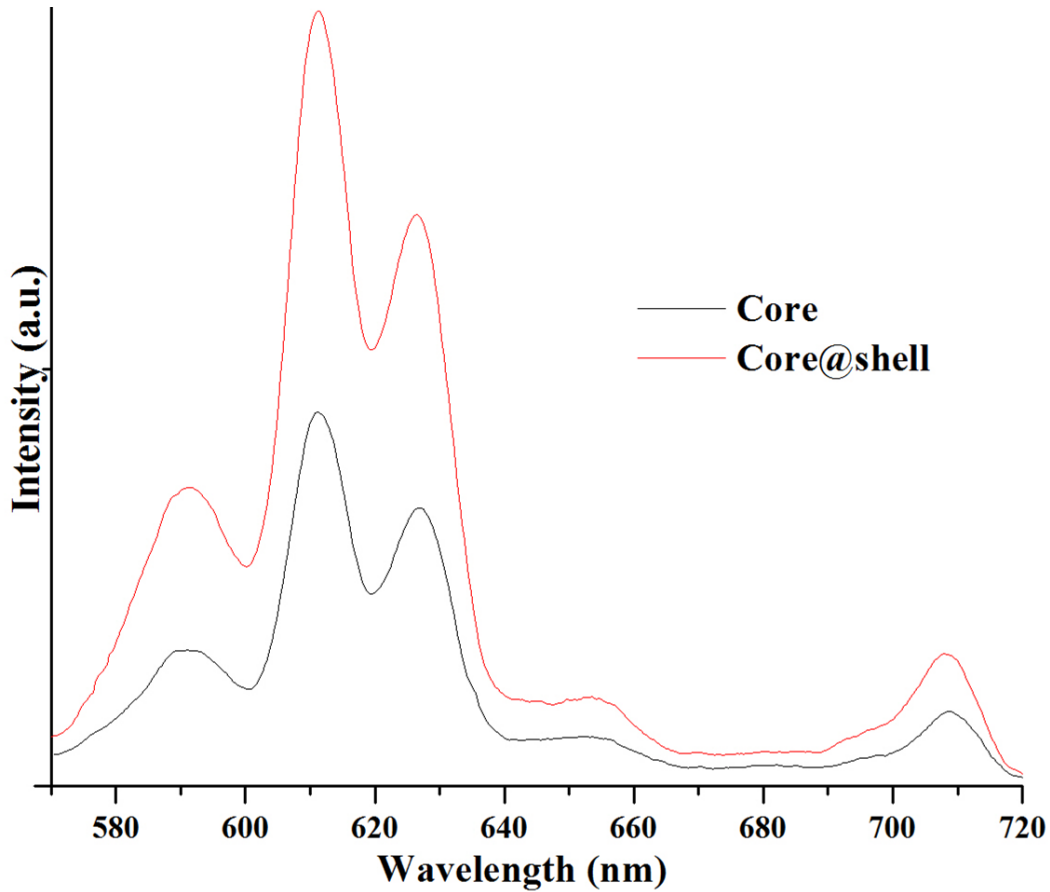
Figure 2.12: Comparison emission spectra of core and core shell nanoparticles.

Nanostructured materials are a new class of materials which provide one of the greatest potentials for improving performance and extended capabilities of products in a number of industrial sectors, including the aerospace, tooling, automotive, recording, cosmetics, electric motor, duplication, and refrigeration industries. Incorporated by this class of materials are multilayers, nanocrystalline materials and nanocomposites. Nanostructured materials have

attracted great interest in recent years because of the unusual mechanical, electrical and optical properties endowed by confining the dimensions of such materials and because of the combination of bulk and surface properties to the overall behavior and a high surface area-to-volume ratio and this characteristic inevitably results in high surface defects density and serious surface recombination. Therefore, RE-doped nanophosphors always have lower luminescence efficiency. YBO_3 has excellent properties such as high VUV transparency, high stability, low synthesis temperature and exceptional optical damage threshold[54,] so, it is an ideal shell material for composite phosphors with core/shell nanostructures.

2.5 Influence Factors

2.5.1 Annealing Temperature

The solubility and reactivity of precursors increase with the increasing annealing/reaction temperature of the solvent medium itself. Moreover, it is known that the viscosity of the molten salt decreases rapidly with an increase of temperature, thereby greatly facilitating the diffusion of precursor species in the solvent itself. In fact, 1) the identity as well as the size of the anion associated with the salt, 2) the solubilities/dissolution rates of the constituent components within the molten salt itself, 3) the precise melting point of either the salt or complex salt mixture used, 4) the heating temperature and duration, as well as 5) the unique morphological (e.g., shape) and chemical composition of the precursors involved are all important, readily controllable factors that influence the growth rate as well as the resultant structural characteristics (i.e., size, shape, and crystallinity) of the as-prepared particles.

Another key issue has been product morphology. Whereas sample had been slowly cooled to room temperature from an annealing temperature of 500 °C, resulting in an effectively longer reaction time consist of big spherical particles. Sample had been prepared at annealing temperature of 600 °C possessed varying the high agglomeration of spherical particles. In fact,

the percentage of spheres increased temperature from 500 °C to 600 °C and finally to get good agglomeration nanospheres in sample with increasing annealing temperature. Hence, these initial observations, which are consistent with our previous data, suggest that higher annealing temperatures and reaction times are conducive to the production of relatively pure; spherically shaped Eu doped $La_2Zr_2O_7$ samples.

The main processing points associated with the MSS method are schematically illustrated in Table 2. Essentially, lanthanide oxide precursors corresponding to the desired compound are mixed with the eutectic mixture of nitrate salt mixture and then annealing at a temperature above the melting point of the salt medium to form a molten flux. At this temperature, precursor molecules disperse, dissociate, rearrange, and then diffuse rapidly throughout the salt. Upon further heating, particles of the desired metal-oxide phase are formed through an initial nucleation step followed by a growth process that is very much dependent upon the identity of the salt species, the quantity of salt used in the reaction medium, the magnitude of the temperature at which the reaction is run, and the reaction duration. After cooling, the salt itself can be typically and rather simply eliminated by washing with deionized water. Upon drying, unagglomerated powders can be routinely obtained after appropriate processing.[55]

Table 2. Flow chart illustrating factors influencing the molten-salt synthesis of transition-metal oxide materials.[55]

Processing step	Factors effect on the nanoparticle
Precursor materials	Initial particle size, shape, geometry, morphology and purity of precursors
Mixing of precursor molecules with salts	Chemical nature and quality of salts, purity of slats
Annealing temperature	Synthesis temperature/ reaction time, heating and cooling rates
Washing of salt mixture with sample	Remaining impurities from salt and precursor components
Drying	Presence of agglomerates

2.5.2 Doping Concentration of Europium

The Eu doping level concentration is a critical factor in photoluminescence enhancement of the $La_2Zr_2O_7$ nanoparticles. When the 10% Eu doped $La_2Zr_2O_7$ nanoparticles exhibits the highest photoluminescence efficiency.

Molten salts have been used as extracts to improve the rates of solid state reactions for a long time and high temperature. The amount of salt is small, typically a few percent of the total weight. In contrast, in molten salt synthesis, a large amount of salt is used as the solvent to control size and shape under a low degree of great soaking. In this sense, molten salt synthesis is different from the flux method, which uses the salt as an additive to increase the reaction rate. As showed in this review, a wide variety of rare-earth ions can be incorporated into several oxides of varying structural complexity and can give strong luminescence up to high temperatures. However, regardless of the similarity in the variation of luminescence lifetime with temperature between many materials, there are several different processes. The processes depend on the activator, the host, and the concentration of the activator. Whereas molten salt can be understand to predict the rates and temperature dependencies of all synthetic process, requiring a tedious experimental approach to identify suitable materials for a given application. In photoluminescence produce to improve for illustration by uses of sensitization efficiency could overcome at higher temperature for zirconia materials used in thermal barrier coatings and related applications.

2.6 Conclusion

$(La_{1-x}Eu_x)_2Zr_2O_7@YBO_3$ core@shell nanoparticles with different doping levels were prepared by sol-gel coating of YBO_3 nanoshell onto the $(La_{1-x}Eu_x)_2Zr_2O_7$ nanoparticles. In the synthesis, the core nanoparticles were synthesized by the molten-salt synthesis procedure because the MSS method is one of the simplest, most versatile, and highly cost-effective

39

approaches available for obtaining crystalline, chemically pure, single-phase nanoscale materials at relative lower temperatures and often in overall shorter reaction times with little residual impurities as compared with conventional solid-state reactions. The mixture of reactant and salt powders is heated at temperatures above the melting point of the salt. The intrinsic scalability, flexibility, and facility of this technique render it attractive for the fabrication of a range of materials. The shell was synthesized by the sol-gel synthesis. Characterizations by means of XRD, TEM, XPS and photoluminescence data confirmed the core-shell-structured phosphor samples with general compositions as $(La_{1-x}Eu_x)_2Zr_2O_7@YBO_3$ were prepared. The $(La_{1-x}Eu_x)_2Zr_2O_7@YBO_3$ nanoparticles shows stronger photoluminescence than the $(La_{1-x}Eu_x)_2Zr_2O_7$ nanoparticles under the same conditions.

CHAPTER III

FUTURE ENDEAVORS

There are many more research investigations that could be carried out concerning the particles that have been produced in the course of this project. Firstly, more work could be done involving the Eu doped lanthanum zirconate nanoparticle systems. It would be interesting to see if the Eu doped lanthanum zirconate nanoparticle systems react in the same way as Eu doped lanthanum zircoante nanoparticle system if treated with different molar ratios. Also, work could be undertaken ammonium stabilizer, to find the optimum concentration and to investigate if aggregation of the samples can be further reduced. The particles produced could be tested to see how luminescence active they are. In theory, the particles should be efficient luminescence as they could have synergistic effects from combining to lanthanide oxides together in the nanoscale, also the lanthanide oxides used are good luminescence[17-18, 21, 29]. The Eu doped lanthanum zirconate nanoparticles produced by molten salt synthesis need further characterization, preferably by thermal analysis of TGA and DSC. However, it did not give information on characteristics such as particle size. HRTEM, SAED patterns analysis would reveal whether the particles had a core-shell configuration. However, it gives information on characteristics such as particle size. These samples need testing in photoluminescence analysis different shell ratios and excitation wavelengths. These samples also need testing for radiation activity. The radiation analysis carried out shows that the core-shells do not change with

41

extended reaction times. This could be preliminarily carried out with radiation analysis, followed up with XRD and TEM analysis.

The synthesis process outlined in this thesis is versatile and can be used for synthesizing other thermo graphic phosphors nanostructures in thermal barrier coatings such as $La_2Zr_2O_7$:Eu, $La_2Hf_2O_7$:Eu, and $Nd_2Zr_2O_7$:Eu is a promising thermographic phosphors. Also, one of our present goals is to prepare Eu doped lanthanum zirconate nanoparticle coated yttrium borate with controlled mean diameter. A low temperature SEM, TEM study will be performed using the as-prepared Eu doped lanthanum zirconate nanoparticle coated yttrium borate become particle size is narrower and low agglomeration.

REFERENCES

1.   Feynman, There's plenty of room at the bottom. *R. P. Eng. Sci.* **1960,** *23* (22).

2.   Reisfeld, R., and Jorgensen, C. K. , Lasers and Excited States of Rare Earths: Berlin. *Springer* **1977**.

3.   Dejneka, M. J.; Streltsov, A.; Pal, S.; Frutos, A. G.; Powell, C. L.; Yost, K.; Yuen, P. K.; Muller, U.; Lahiri, J., Rare earth-doped glass microbarcodes. *P Natl Acad Sci USA* **2003,** *100* (2), 389-393.

4.   Tyagi, B. P. M. a. A. K., Pyrochlores-Potential multifunctional materials. *Barc Newsletter* **2010,** (313).

5.   Mao, Y.; Guo, X.; Huang, J. Y.; Wang, K. L.; Chang, J. P., Luminescent Nanocrystals with $A_2B_2O_7$ Composition Synthesized by a Kinetically Modified Molten Salt Method. *J Phys Chem C* **2009,** *113* (4), 1204-1208.

6.   Weller, M. T.; Hughes, R. W.; Rooke, J.; Knee, C. S.; Reading, J., The pyrochlore family - a potential panacea for the frustrated perovskite chemist. *Dalton Transactions* **2004,** (19), 3032-3041.

7.   C.A. Mims, A. J. J., R.B. Hall, J.T. Lewandowski, Methane Oxidative Coupling over Nonstoichiometric Bismuth-Tin Pyrochlore Catalysts Original Research Article. *Journal of Catalysis* **1995,** *153* (2), 197-207.

8.   Bansal, N. P.; Zhu, D., Effects of doping on thermal conductivity of pyrochlore oxides for advanced thermal barrier coatings. *Materials Science and Engineering: A* **2007,** *459* (1-2), 192-195.

9.   Xiang, J.; Chen, S.; Huang, J.; Zhang, H.; Zhao, X., Phase structure and thermophysical properties of co-doped $La_2Zr_2O_7$ ceramics for thermal barrier coatings. *Ceramics International* **2012,** *38* (5), 3607-3612.

10.   Mizoguchi H, E. H., Woodward PM., Probing the electronic structures of ternary perovskite and pyrochlore oxides containing Sn^{4+} or Sb^{5+}. *Inorg Chem.* **2004,** *43* (5), 1667-80.

11.   Lu, Z.; Wang, J.; Tang, Y.; Li, Y., Synthesis and photoluminescence of Eu^{3+}-doped Y$_2$Sn$_2$O$_7$ nanocrystals. *Journal of Solid State Chemistry* **2004,** *177* (9), 3075-3079.

12.   Sickafus, K. E.; Minervini, L.; Grimes, R. W.; Valdez, J. A.; Ishimaru, M.; Li, F.; McClellan, K. J.; Hartmann, T., Radiation tolerance of complex oxides. *Science* **2000,** *289* (5480), 748-51.

13.   Yasutake TeraokaCorresponding author contact information; Ken-ichiro Torigoshi; Hidetoshi Yamaguchi; Takashi Ikeda; Kagawa, S., Direct decomposition of nitric oxide over stannate pyrochlore oxides- relationship between solid-state chemistry and catalytic activity. *Journal of Molecular Catalysis A: Chemical* **2000,** *155* (1–2), 73–80.

14.   Sohn, J. M.; Kim, M. R.; Woo, S. I., The catalytic activity and surface characterization of Ln$_2$B$_2$O$_7$ (Ln=Sm, Eu, Gd and Tb; B=Ti or Zr) with pyrochlore structure as novel CH$_4$ combustion catalyst. *Catalysis Today* **2003,** *83* (1-4), 289-297.

15.   Sarohan Park, H. J. H. a. J. M., Catalytic Combustion of Methane over Rare Earth Stannate Pyrochlore. *Catalysis Letters* **2003,** *87* (3–4), 219-223.

16.   Lumpkin, G. R.; Whittle, K. R.; Rios, S.; Smith, K. L.; Zaluzec, N. J., Temperature dependence of ion irradiation damage in the pyrochlores La$_2$Zr$_2$O$_7$ and La$_2$Hf$_2$O$_7$. *Journal of Physics: Condensed Matter* **2004,** *16* (47), 8557-8570.

17.   Shinobu Fujihara, K. T., Multiband Orange-Red Luminescence of Eu^{3+} Ions Based on the Pyrochlore-Structured Host Crystal. *Chem. Mater.* **2005,** *17* (22), 5587–5593.

18.   Zhang, A.; Lü, M.; Zhou, G.; Wang, S.; Zhou, Y., Combustion synthesis and photoluminescence of Eu^{3+}, Dy^{3+}-doped La$_2$Zr$_2$O$_7$ nanocrystals. *Journal of Physics and Chemistry of Solids* **2006,** *67* (11), 2430-2434.

19.   Chen, H.; Gao, Y.; Liu, Y.; Luo, H., Coprecipitation synthesis and thermal conductivity of La$_2$Zr$_2$O$_7$. *Journal of Alloys and Compounds* **2009,** *480* (2), 843-848.

20.   Wang, X.; Zhu, Y.; Zhang, W., Preparation of lanthanum zirconate nano-powders by Molten Salts method. *Journal of Non-Crystalline Solids* **2010,** *356* (20-22), 1049-1051.

21.   Zhang, A.; Lü, M.; Yang, Z.; Zhou, G.; Zhou, Y., Systematic research on RE$_2$Zr$_2$O$_7$ (RE=La, Nd, Eu and Y) nanocrystals: Preparation, structure and photoluminescence characterization. *Solid State Sciences* **2008,** *10* (1), 74-81.

22.   Wang, S. M.; Xiu, Z. L.; Lü, M. K.; Zhang, A. Y.; Zhou, Y. Y.; Yang, Z. S., Combustion synthesis and luminescent properties of Dy^{3+}-doped $La_2Sn_2O_7$ nanocrystals. *Materials Science and Engineering: B* **2007,** *143* (1-3), 90-93.

23.   K Koteswara Rao, T. B., M Vithal, G.Y.S.K Swamy, K Ravi Kumar, Preparation and characterization of bulk and nano particles of $La_2Zr_2O_7$ and $Nd_2Zr_2O_7$ by sol–gel method. *Material letters* **2002,** *54*, 205-210.

24.   Hirayama, M.; Sonoyama, N.; Yamada, A.; Kanno, R., Relationship between structural characteristics and photoluminescent properties of $(La_{1-x}Eu_x)_2M_2O_7$ (M=Zr, Hf, Sn) pyrochlores. *Journal of Luminescence* **2008,** *128* (11), 1819-1825.

25.   D ChenA, R. X., Hydrothermal Synthesis and Characterization of $La_2M_2O_7$ (M = Ti, Zr) Powders. *Materials Research Bulletin* **1998,** *33* (3), 409–417.

26.   Diane K. Williams, B. B., and Brian M. Tissue, James M. McHale, Preparation and Fluorescence Spectroscopy of Bulk Monoclinic Eu^{3+}-Y_2O_3 and Comparison to Eu^{3+}-Y_2O_3 Nanocrystals. *J. Phys. Chem. B* **1998,** *102* (6), 916–920.

27.   Osvaldo A Serra, S. A. C., Renata R Ishiki, A new procedure to obtain Eu^{3+} doped oxide and oxosalt phosphors. *Journal of Alloys and Compounds* **2000,** *303–304* (24), 316–319.

28.   Tian, L.; Yu, B.-Y.; Pyun, C.-H.; Park, H. L.; Mho, S.-i., New red phosphors $BaZr(BO_3)_2$ and $SrAl_2B_2O_7$ doped with Eu^{3+} for PDP applications. *Solid State Communications* **2004,** *129* (1), 43-46.

29.   Wang, S. M.; Lu, M. K.; Zhou, G. J.; Zhou, Y. Y.; Zhang, H. P.; Wang, S. F.; Yang, Z. S., Synthesis and luminescence properties of $La_{2-x}RE_xSn_2O_7$ (RE=Eu and Dy) phosphor nanoparticles. *Materials Science and Engineering: B* **2006,** *133* (1-3), 231-234.

30.   Uno, M.; Kosuga, A.; Okui, M.; Horisaka, K.; Muta, H.; Kurosaki, K.; Yamanaka, S., Photoelectrochemical study of lanthanide zirconium oxides, $Ln_2Zr_2O_7$ (Ln=La, Ce, Nd and Sm). *Journal of Alloys and Compounds* **2006,** *420* (1-2), 291-297.

31.   Karl A. Gschneidner, J., Jean-Claude Bünzli, Vitalij K. Pecharsky, Handbook on the Physics and Chemistry of Rare Earths. *41*.

32.   Levin, E. M.; Roth, R. S.; Martin, J. B., Polymorphism of Abo_3 Type Rare Earth Borates. *Am Mineral* **1961,** *46* (9-10), 1030-1055.

33.   Zhu, H.; Hu, H.; Wang, Z.; Zuo, D., Synthesis of YVO$_4$:Eu^{3+}/YBO$_3$ Heteronanostructures with Enhanced Photoluminescence Properties. *Nanoscale Research Letters* **2009,** *4* (9), 1009-1014.

34.   Caruso, R. A.; Susha, A.; Caruso, F., Multilayered titania, silica, and Laponite nanoparticle coatings on polystyrene colloidal templates and resulting inorganic hollow spheres. *Chem Mater* **2001,** *13* (2), 400-409.

35.   Kemin Wang, W. T., Xiaoxiao He, Biomedical Applications Based on Core-Shell Nanoparticles. *IEEE-EMBS* **2005**, 717-719.

36.   Cuikun Lin, D. K., Xiaoming Liu, Huan Wang, Min Yu, and Jun Lin, Monodisperse and Core−Shell-Structured SiO$_2$@YBO$_3$,Eu^{3+} Spherical Particles Synthesis and Characterization. *Inorg. Chem* **2007,** *46*, 2674–2681.

37.   Kalele, S.; Gosavi, S. W.; Urban, J.; Kulkarni, S. K., Nanoshell particles: synthesis, properties and applications. *Current Science* **2006,** *91* (8), 1038-1052.

38.   Chaudhuri, R. G.; Paria, S., Core/Shell Nanoparticles: Classes, Properties, Synthesis Mechanisms, Characterization, and Applications. *Chem Rev* **2012,** *112* (4), 2373-2433.

39.   Zhu, H. L.; Hu, H. H.; Wang, Z. K.; Zuo, D. A. T., Synthesis of YVO$_4$:Eu^{3+}/YBO$_3$ Heteronanostructures with Enhanced Photoluminescence Properties. *Nanoscale Res Lett* **2009,** *4* (9), 1009-1014.

40.   Zhou, J.; Zhang, S. W.; Qiao, X. G.; Li, X. Q.; Wu, L. M., Synthesis of SiO$_2$/poly(styrene-co-butyl acrylate) nanocomposite microspheres via miniemulsion polymerization. *J Polym Sci Pol Chem* **2006,** *44* (10), 3202-3209.

41.   Wang, J.; Shi, T. J.; Jiang, X. C., Synthesis and Characterization of Core-shell ZrO$_2$/PAAEM/PS Nanoparticles. *Nanoscale Research Letters* **2008,** *4* (3), 240-246.

42.   WEST, L. L. H. a. J. K., The sol-gel process. *Chem. Rev.* **1990,** *90*, 33-72.

43.   Brinker, C. J. S., G. W., Sol-Gel Science: The Physics and Chemistry of Sol-Gel Processing. *Academic Press, Inc.: San Diego* **1990,** *199*, 1-908.

44.   Demazeau, G., Solvothermal processes: new trends in Materials Chemistry. *J Phys Conf Ser* **2008,** *121*.

45.   Crepaldi, E. L.; Pavan, P. C.; Valim, J. B., Comparative study of the coprecipitation methods for the preparation of layered double hydroxides. *J Brazil Chem Soc* **2000,** *11* (1), 64-70.

46.   Ke Zhang, B.-J. P., Fei-Fei Fang and Hyoung Jin Choi, Sonochemical Preparation of Polymer Nanocomposites. *Molecules* **2009,** *14*, 2095-2110.

47.   Tong, Y.; Wang, Y.; Yu, Z.; Wang, X.; Yang, X.; Lu, L., Preparation and characterization of pyrochlore $La_2Zr_2O_7$ nanocrystals by stearic acid method. *Materials Letters* **2008,** *62* (6-7), 889-891.

48.   Zhenggui, L., Chunsheng, Jialu, Xiaocheng, and Chunhua, Size-Dependent Chromaticity in YBO_3:Eu Nanocrystals: Correlation with Microstructure and Site Symmetry. *J. Phys. Chem. B106* **2002,** *106* (41), 10610–10617.

49.   Ren, M.; Lin, J. H.; Dong, Y.; Yang, L. Q.; Su, M. Z.; You, L. P., Structure and phase transition of $GdBO_3$. *Chem Mater* **1999,** *11* (6), 1576-1580.

50.   Jia, G.; You, H.; Liu, K.; Zheng, Y.; Guo, N.; Jia, J.; Zhang, H., Highly Uniform YBO_3 Hierarchical Architectures: Facile Synthesis and Tunable Luminescence Properties. *Chemistry - A European Journal* **2010,** *16* (9), 2930-2937.

51.   Singh, N. S.; Ningthoujam, R. S.; Devi, L. R.; Yaiphaba, N.; Sudarsan, V.; Singh, S. D.; Vatsa, R. K.; Tewari, R., Luminescence study of Eu^{3+} doped $GdVO_4$ nanoparticles: Concentration, particle size, and core/shell effects. *Journal of Applied Physics* **2008,** *104* (10), 104307-1 to 104307-9.

52.   Singh, L. R.; Ningthoujam, R. S., Critical view on energy transfer, site symmetry, improvement in luminescence of Eu^{3+}, Dy^{3+} doped YVO_4 by core-shell formation. *Journal of Applied Physics* **2010,** *107* (10), 104304-1 to 104304-6.

53.   Zhu, H.; Yang, D.; Zhu, L.; Li, D.; Chen, P.; Yu, G., Hydrothermal Synthesis and Photoluminescence Properties of $La_{2-x}Eu_xSn_2O_7$(x=0-2.0) Nanocrystals. *Journal of the American Ceramic Society* **2007,** *90* (10), 3095-3098.

54.   Tukia, M.; Hölsä, J.; Lastusaari, M.; Niittykoski, J., Eu^{3+} doped rare earth orthoborates, RBO_3 (R=Y, La and Gd), obtained by combustion synthesis. *Optical Materials* **2005,** *27* (9), 1516-1522.

55.   Mao, Y.; Park, T. J.; Zhang, F.; Zhou, H.; Wong, S. S., Environmentally friendly methodologies of nanostructure synthesis. *Small* **2007,** *3* (7), 1122-39.

BIOGRAPHICAL SKETCH

Suresh Babu Alaparthi, was born in 1978 in Andhra Pradesh, India. He obtained his high school from A.T.P.M High School in 1993. He obtained his college degree from NVR junior college. Then he attended Nagarjuna University in 1998, for his bachelor's degree in Chemistry. He finished his studies in 2003 and obtained master's degree in Mathematics. He moved to the US in 2010 and he was accepted to the University of Texas-Pan American (UTPA) in 2010 in order to pursue a master's degree in chemistry. There he began to work as graduate assistant while working on research with Dr. Yuanbing Mao on his thesis topic, synthesis and luminescence properties of core-shell structured $(La_{1-x}Eu_x)_2Zr_2O_7@YBO_3$ spherical nanoparticles. He finished his studies in December 2012.

His permanent address is:

Suresh Babu Alaparthi

F/O Sambaiah Alaparthi

Pedda Reddy Palem

Narasarao Pet

Guntur

Andhra Pradesh

India.